PAPER • OPEN ACCESS

The chiral biquadratic pair interaction

New Journal of Physics
The open access journal at the forefront of physics

Deutsche Physikalische Gesellschaft DPG
IOP Institute of Physics

Published in partnership with: Deutsche Physikalische Gesellschaft and the Institute of Physics

OPEN ACCESS

RECEIVED
24 April 2019

REVISED
17 July 2019

ACCEPTED FOR PUBLICATION
25 July 2019

PUBLISHED
9 August 2019

PAPER

The chiral biquadratic pair interaction

Sascha Brinker[1,2,3], **Manuel dos Santos Dias**[1] and **Samir Lounis**[1]

[1] Peter Grünberg Institut and Institute for Advanced Simulation, Forschungszentrum Jülich & JARA, D-52425, Jülich, Germany
[2] Department of Physics, RWTH Aachen University, D-52056, Aachen, Germany
[3] Author to whom any correspondence should be addressed.

E-mail: s.brinker@fz-juelich.de **and** s.lounis@fz-juelich.de

Keywords: magnetic interactions, spin–orbit coupling, electronic structure, non-collinear magnetism

Abstract

Magnetic interactions underpin a plethora of magnetic states of matter, hence playing a central role both in fundamental physics and for future spintronic and quantum computation devices. The Dzyaloshinskii–Moriya interaction, $\mathbf{D}_{ij} \cdot (\mathbf{S}_i \times \mathbf{S}_j)$, being chiral and driven by relativistic effects, leads to the stabilization of highly-noncollinear spin textures such as skyrmions, which thanks to their topological nature are promising building blocks for magnetic data storage and processing elements. Here, we reveal and study a new chiral pair interaction, $\mathbf{C}_{ij} \cdot (\mathbf{S}_i \times \mathbf{S}_j)(\mathbf{S}_i \cdot \mathbf{S}_j)$, which is the biquadratic equivalent of the DMI. First, we derive this interaction and its guiding principles from a microscopic model, and we connect the atomistic form to the micromagnetic one. Second, we study its properties in the simplest prototypical systems, magnetic 3*d* transition metal dimers deposited on the Pt(111), Pt(100), Ir(111), and Re(0001) surfaces, resorting to systematic first-principles calculations. Lastly, we discuss its importance and implications not only for magnetic dimers but also for extended systems, namely one-dimensional spin spirals and complex two-dimensional magnetic structures, such as a nanoskyrmion lattice found in an Fe monolayer on Ir(111).

1. Introduction

Starting from the seminal work of Heisenberg [1], magnetic materials are often described by bilinear isotropic magnetic interactions, $J_{ij}\ \mathbf{S}_i \cdot \mathbf{S}_j$. However, a wealth of complex spin-textures were discovered over the last century that called for the enrichment of the original Heisenberg model with various other types of interactions (see e.g. [2–11]). The magnetism of ^{3}He is a striking example, being dominated by higher-order isotropic interactions [12] which can be derived from the Hubbard model at half-filling [13–16] or from Kondo-lattice models [17–19]. These interactions, such as the isotropic biquadratic interaction $B_{ij}(\mathbf{S}_i \cdot \mathbf{S}_j)^2$ and the related three- and four-site interactions, introduce nonlinear effects into the Heisenberg model. An important consequence is that different spin spirals, characterized by a wavevector $\mathbf{Q}$, can be combined into lower-energy multiple-Q-states, as the higher-order interactions invalidate the superposition principle. Prominent examples are the antiferromagnetic *uudd*-state (a 2Q-state) [20, 21] and the 3Q-state [22]. Interestingly, this 3Q-state (also magnetic skyrmions [23, 24] and bobbers [25, 26]) is a noncoplanar magnetic state that hosts interesting Berry-phase physics arising from its non-vanishing scalar spin chirality $\mathbf{S}_i \cdot (\mathbf{S}_j \times \mathbf{S}_k)$, such as topological orbital ferromagnetism and Hall effects [27–31].

The concept of vector spin chirality is embodied by the antisymmetric bilinear Dzyaloshinskii–Moriya interaction (DMI), $\mathbf{D}_{ij} \cdot (\mathbf{S}_i \times \mathbf{S}_j)$ [3, 4], which arises due to the combination of spin–orbit coupling and absence of spatial inversion symmetry. The DMI lifts the energy degeneracy of magnetic spirals with opposite vector spin chirality, $\mathbf{S}_i \times \mathbf{S}_j$, thus stabilizing magnetic structures of well-defined rotational sense, such as chiral spin spirals [32, 33] and magnetic skyrmions [23, 24]. The competition between the DMI and the symmetric anisotropic exchange was recently found to explain the magnetic stability of decorated Fe trimers on the Pt(111) surface [34]. The intricate interplay of higher-order and anisotropic bilinear magnetic interactions generates various magnetic states: conical spin spirals [35] and more complex magnetic structures [31, 36, 37], such as an intricate nanoskyrmion lattice for a monolayer of Fe on the Ir(111) surface [38].

In this work, we utilize a microscopic model combined with first-principles calculations to introduce and characterize a new kind of spin–orbit-driven magnetic pair interaction, the chiral biquadratic interaction (CBI). It has the form $\mathbf{C}_{ij} \cdot (\mathbf{S}_i \times \mathbf{S}_j)(\mathbf{S}_i \cdot \mathbf{S}_j)$. Like the DMI, this is a unidirectional interaction which is linear in the spin–orbit coupling, and so it is governed by the magnitude and orientation of the CBI vector $\mathbf{C}_{ij}$. We demonstrate that this vector obeys the same symmetry rules as the DMI [4, 39–41], and derive its micromagnetic limit. Like the isotropic biquadratic interaction, the CBI couples twice the same pair of magnetic moments. Noteworthy, the CBI is not chiral on its own, but supports a definite chirality based on the nature of the non-chiral bilinear exchange interaction, being ferromagnetic or antiferromagnetic, and the chiral DMI. After systematic investigations on magnetic dimers made of 3*d* elements on various surfaces with strong spin–orbit coupling, namely Pt(111), Pt(001), Ir(111) and Re(0001) surfaces, we find that the CBI can be comparable in magnitude to the DMI. Lastly, we explore the implications of the CBI for magnetic structures in one and two dimensions.

2. Methods

2.1. Density functional theory

We performed systematic density functional theory calculations with the full-potential Korringa–Kohn–Rostoker (KKR) Green function method [42]. Exchange and correlation effects are treated in the local spin density approximation as parametrized by Vosko *et al* [43], and spin–orbit coupling is added to the scalar-relativistic approximation [44]. The pristine surfaces are modeled by a slab of 22 layers (except for Pt(111) for which 40 layers were used) with the experimental lattice constants with open boundary conditions in the stacking direction, and surrounded by two vacuum regions. No relaxation of the surface layer of the pristine surface is considered, as it was shown to be negligible [45]. We use 150×150 k-points in the two-dimensional Brillouin zone, and the angular momentum expansions for the scattering problem are carried out up to $\ell_{\max} = 3$. In the next step, we utilize an embedding method to place each dimer on the fcc-like threefold hollow position of Pt(111) and Ir(111), on the fourfold hollow sites on the Pt(001) surface, and on the hcp-like threefold hollow site of Re(0001). The embedding region consists of a spherical cluster around each magnetic adatom including nearest-neighbor surface atoms.

We found this to be sufficient to adequately capture the indirect contribution to the magnetic interactions arising from the induced spin polarization of the surface atoms. The appropriate structural relaxations of each dimer towards the surface were obtained with the plane-wave code Quantum Espresso [46], using ultrasoft scalar relativistic pseudopotentials [47] with the PBEsol functional [48], and considering a 4×4 supercell with 5 substrate layers (more details and structural information are given in appendix A). All calculations were performed on the supercomputer JURECA at the Forschungszentrum Jülich [49].

2.2. Mapping DFT to an atomistic spin model—the torque method

To map the first-principles calculations to an atomistic spin model we adopted the method of constraining fields [50]. The net magnetic moment for each atom in the dimer is defined by averaging the spin magnetization density over its atomic cell, $\mathbf{m}_i = \int \mathrm{d}\mathbf{r}\, \mathbf{m}_i(\mathbf{r})$. The orientations of the magnetic moments $\mathbf{S}_i = \mathbf{m}_i/|\mathbf{m}_i|$ play the role of emergent degrees of freedom that can be used to define an atomistic spin model,

$$E_{\mathrm{DFT}}[\{\mathbf{S}\}] = \sum_i \sum_{\alpha,\beta} K_i^{\alpha\beta} S_i^\alpha S_i^\beta + \frac{1}{2} \sum_{i,j} \sum_{\alpha,\beta} J_{ij}^{\alpha\beta} S_i^\alpha S_j^\beta + \ldots \tag{1}$$

To determine the energy of a target magnetic configuration, the total energy functional is augmented by a Zeeman term enforcing the constraint,

$$E_{\mathrm{cDFT}}[\{\mathbf{S}\}] = E_{\mathrm{DFT}}[\{\mathbf{S}\}] - \sum_i \mathbf{b}_i \cdot \int \mathrm{d}\mathbf{r}\, \mathbf{m}_i(\mathbf{r}). \tag{2}$$

The constraining magnetic field is transverse to the orientation of the local magnetic moment, $\mathbf{b}_i \cdot \mathbf{S}_i = 0$, and it opposes the magnetic force that acts on it if the magnetic structure is not a stationary point of the total energy functional,

$$\frac{\delta E_{\mathrm{cDFT}}[\{\mathbf{S}\}]}{\delta \mathbf{S}_i} = \frac{\delta E_{\mathrm{DFT}}[\{\mathbf{S}\}]}{\delta \mathbf{S}_i} - \mathbf{b}_i\, |\mathbf{m}_i| = \mathbf{0}. \tag{3}$$

The induced moments in the surface atoms are allowed to relax without any constraint. The model parameters are then determined by linear least-squares fitting the constraining fields obtained for a set of self-consistent magnetic configurations to the form of the magnetic force supplied by the atomistic spin model. The magnetic configurations for the dimers have been chosen using a Lebedev grid [51] containing 14 directions for each atom, which is well-suited to describe spherical harmonics up to $\ell = 2$, resulting in a total of $14^2 = 196$ configurations, which using symmetry arguments (time-reversal invariance of the magnetic energy plus the spatial symmetries that apply on different surfaces) the number of configurations can be further reduced to 56 for (111) and (0001) surfaces and to 36 for (001) surfaces.

3. Results

3.1. Systematic microscopic derivation of higher-order interactions

The benefits of studying the properties of the magnetic interactions starting from a microscopic model are well-illustrated by the case of the DMI. Although phenomenological arguments completely determine the form and symmetry properties of the DMI [3], the microscopic analysis of Moriya [4] and later on the intuitive picture proposed by Fert and Lévy [39, 40] have clarified the main ingredients that underpin this interaction. We thus begin by introducing a generic model of the electronic structure of the magnetic material, and then outline how one can systematically extract all kinds of magnetic interactions from the electronic grand potential.

3.1.1. Microscopic model

The microscopic hamiltonian that we consider has three contributions: $\mathcal{H} = \mathcal{H}^0 + \mathcal{H}^{\rm mag} + \mathcal{H}^{\rm soc}$. Here $\mathcal{H}^0$ contains all spin-independent contributions, $\mathcal{H}^{\rm mag} = \sum_i U_i\, \mathbf{S}_i \cdot \boldsymbol{\sigma}$ is the local exchange coupling of strength U_i between the direction of the magnetic moment $\mathbf{S}_i$ on site i and the electronic spin $\boldsymbol{\sigma}$, and $\mathcal{H}^{\rm soc} = \sum_a \lambda_a\, \mathbf{L}_a \cdot \boldsymbol{\sigma}$ is the atomic spin–orbit coupling of strength λ_a on site a between the electron spin and its atomic orbital angular momentum $\mathbf{L}_a$. Grouping the spin-dependent terms into $\Delta\mathcal{H} = \mathcal{H}^{\rm mag} + \mathcal{H}^{\rm soc}$, it is straightforward to derive a formal power series for the electronic grand potential (see appendix B),

$$\begin{aligned}\Omega &= \Omega^0 - \frac{1}{\pi}\,\mathrm{Im}\int \mathrm{d}E\, f(E;\,\mu)\sum_p \frac{1}{p}\,\mathrm{Tr}\,[\Delta\mathcal{H}\, G^0(E)]^p \\ &= \Omega^0 + \Omega^{\rm soc} + \sum_p \sum_{k=1}^{p/2} \Omega^{p,2k}[\{\mathbf{S}_i\}]. \end{aligned} \tag{4}$$

Here Ω^0 is the contribution to the grand-canonical potential from the spin-independent $\mathcal{H}^0$, and $G^0(E) = (E - \mathcal{H}^0)^{-1}$ is the corresponding retarded Green function. The contributions arising solely from spin–orbit coupling are collected in $\Omega^{\rm soc}$, and the terms that depend on the magnetic moments are given by $\Omega^{p,2k}[\{\mathbf{S}_i\}]$. The Fermi–Dirac distribution for energy E and chemical potential μ is given by $f(E;\mu)$, and the trace is over all sites, orbitals and spin degrees of freedom. We reiterate that this expansion is a formal power series, so neither the magnetic hamiltonian, $\mathcal{H}^{\rm mag}$, nor the spin–orbit coupling part, $\mathcal{H}^{\rm soc}$, have to be considered as perturbations. Our goal is to systematically uncover the simplest contributions that generate a magnetic interaction of a given form, not to compute its microscopic value from this model, so the non-perturbative nature of the expansion poses no difficulties.

3.1.2. Diagrammatic rules

Only a subset of the terms contained in $\Omega^{p,2k}[\{\mathbf{S}_i\}]$ are of interest for the purpose of identifying the possible types of magnetic interactions. As detailed in appendix B, these can be represented by prototypical diagrams for all kinds of magnetic interactions, from magnetocrystalline anisotropies to pair interactions or many-site interactions. Each diagram contain p vertices connected by p lines. The vertices in a prototypical diagram must correspond to spatially distinct sites, and the lines represent connections between the sites through G^0. Each diagram contains $2k$ magnetic sites and p–$2k$ spin–orbit sites. A link between two magnetic sites is denoted by a solid line, while a link between a magnetic site and a spin–orbit site is marked by a dashed line. A magnetic site cannot appear consecutively (i.e. a line cannot close on itself), and two consecutive spin–orbit sites (distinct or not) are also excluded. In this work we focus on interactions involving two magnetic sites, and the corresponding prototypical diagrams up to fourth order in the magnetic sites and first order in spin–orbit coupling are shown in figures 1(a)–(d).

3.1.3. Prototypical diagrams

It is a simple matter to extract the form of the magnetic interactions from each prototypical diagram, by using the properties of traces of Pauli matrices. The derivations and the forms of the coupling coefficients can be found in appendix B. The first and simplest diagram is given in figure 1(a) and translates into the isotropic bilinear exchange interaction $\frac{1}{2}\sum_{i,j} J_{ij}\, \mathbf{S}_i \cdot \mathbf{S}_j$. Attaching one spin–orbit site to the diagram of figure 1(a) results in the diagram shown in figure 1(b). This generates the DMI, $\frac{1}{2}\sum_{i,j}\mathbf{D}_{ij} \cdot (\mathbf{S}_i \times \mathbf{S}_j)$. The structure of this diagram is identical to the third-order perturbation theory developed by Fert and Lévy [39, 40]. The DMI vector is determined by the properties and geometrical arrangement of the spin–orbit sites, $\mathbf{D}_{ij} = \sum_a \mathbf{D}_{ij,a}$. Due to the cross product form, it favors magnetic structures with a definite vector chirality. The next diagram is shown in figure 1(c) and leads to the isotropic biquadratic interaction, $\frac{1}{2}\sum_{i,j} B_{ij}(\mathbf{S}_i \cdot \mathbf{S}_j)^2$. The diagrams with the same number of lines but connecting either three or four different magnetic sites lead to the isotropic 4-spin 3-site and 4-spin 4-site interactions, respectively (see appendix B). Lastly, we find a new kind of magnetic interaction from the prototypical diagram shown in figure 1(d):

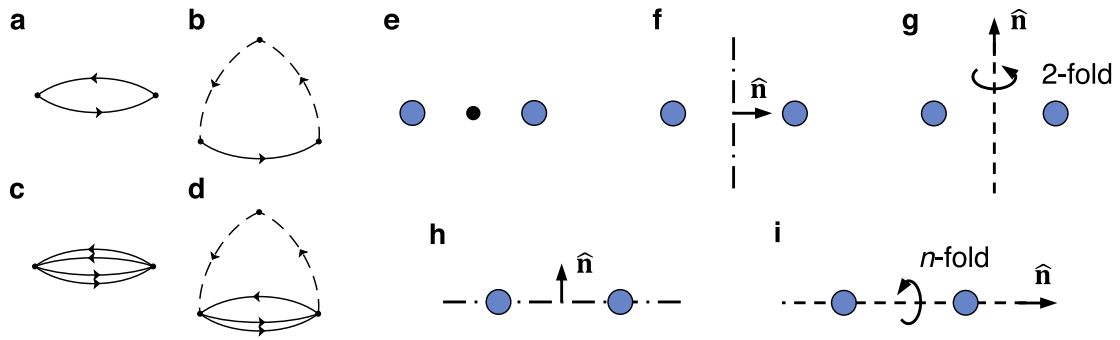

Figure 1. Feynman diagrams and symmetry operations used for the microscopic derivation of the magnetic interactions. (a)–(d) Prototypical diagrams for pair interactions up to fourth order in the magnetic hamiltonian and first order in the spin–orbit hamiltonian. Green functions connecting sites are represented by solid lines if both sites are magnetic and by dashed lines if one is a spin–orbit site. The five different symmetry operations being illustrated are: (e) inversion center in-between the two magnetic sites; (f) mirror plane perpendicular to their bond; (g) two-fold rotation perpendicular to their bond; (h) mirror plane containing both magnetic sites; and (i) n-fold rotation axis containing both magnetic sites. The unit vectors $\hat{\mathbf{n}}$ represent either the rotation axis or the normal to the mirror plane.

$$(1\mathrm{d}) \;\rightarrow\; \frac{1}{2}\sum_{i,j}\mathbf{C}_{ij}\cdot(\mathbf{S}_i\times\mathbf{S}_j)(\mathbf{S}_i\cdot\mathbf{S}_j). \tag{5}$$

We name it the CBI, as it is an antisymmetric 4-spin 2-site interaction generated by an additional spin–orbit site. It thus combines the isotropic scalar product $\mathbf{S}_i\cdot\mathbf{S}_j$ with the chiral coupling $\mathbf{C}_{ij}\cdot(\mathbf{S}_i\times\mathbf{S}_j)$ defined by the CBI vector $\mathbf{C}_{ij}=\sum_a\mathbf{C}_{ij,a}$, which is generated by the spin–orbit sites. This is our main quantity of interest and its properties will be discussed in detail in this paper. The diagrams with the same number of lines but connecting either three or four different magnetic sites lead to the chiral 4-spin 3-site and 4-spin 4-site interactions, respectively (see appendix B).

3.1.4. Symmetry rules

We next study what are the properties of the newly-found CBI vector, $\mathbf{C}_{ij}$, by comparison with those of the DMI vector, $\mathbf{D}_{ij}$. Given a pair of magnetic sites i and j connected with the vector $\mathbf{R}_{ij}$, there are five relevant symmetries, which are illustrated in figures 1(e)–(i). Within the picture of the prototypical diagrams, these symmetry operations are combinations of local transformations at each site (e.g. a rotation or a mirroring) and permutations of the sites. Importantly, symmetry dictates what is the spatial arrangement of the spin–orbit sites around the pair of magnetic sites. One can then relate the diagrams connecting the pair of magnetic sites to each spin–orbit site, noting that the orbital angular momentum operator transforms as a pseudovector, and from this derive the symmetry rules for each magnetic interaction. For the DMI vector, these symmetries lead to the so-called Moriya's rules [4, 40, 41]. These rules are, for each symmetry operation shown in figures 1(e)–(i): (e) $\mathbf{D}_{ij}=0$, (f) $\mathcal{P}^{\parallel}_{\hat{\mathbf{n}}}\mathbf{D}_{ij}=0$, (g) $\mathcal{P}^{\parallel}_{\hat{\mathbf{n}}}\mathbf{D}_{ij}=0$, (h) $\mathcal{P}^{\perp}_{\hat{\mathbf{n}}}\mathbf{D}_{ij}=0$, and (i) $\mathcal{P}^{\perp}_{\hat{\mathbf{n}}}\mathbf{D}_{ij}=0$ (see appendix C). The vanishing components of the DMI vector are those either parallel or perpendicular to $\hat{\mathbf{n}}$, which represents either the rotation axis or the normal to the mirror plane. It follows naturally from comparing the structure of the prototypical diagrams for the DMI and the CBI that precisely the same rules apply to the CBI vector, $\mathbf{C}_{ij}$. The two vectors do not have to be collinear, notably if the only applicable symmetry is a mirror plane perpendicular to the bond direction.

3.1.5. Connection to a phenomenological model

Another advantage of our approach is apparent if we consider the appropriate phenomenological model for the magnetic interactions. To illustrate this point, we consider the most general spin model containing only bilinear and biquadratic pair interactions:

$$\mathcal{H}^{\mathrm{pair}}=\frac{1}{2}\sum_{i,j}\sum_{\alpha,\beta}J_{ij}^{\alpha\beta}S_i^{\alpha}S_j^{\beta}+\frac{1}{2}\sum_{i,j}\sum_{\alpha,\beta,\gamma,\delta}B_{ij}^{\alpha\beta\gamma\delta}S_i^{\alpha}S_j^{\beta}S_i^{\gamma}S_j^{\delta}. \tag{6}$$

The bilinear interactions are described by a rank-2 cartesian tensor $J_{ij}^{\alpha\beta}$ (9 parameters), which contains the isotropic pair interaction given by $J_{ij}\,\mathbf{S}_i\cdot\mathbf{S}_j$ (1 parameter), the DMI given by $\mathbf{D}_{ij}\cdot(\mathbf{S}_i\times\mathbf{S}_j)$ (3 parameters), and the remaining five parameters describe the symmetric bilinear pair anisotropy. The biquadratic interactions are described by a rank-4 cartesian tensor $B_{ij}^{\alpha\beta\gamma\delta}$ (81 parameters), and are not straightforward to classify. The number of independent elements of the biquadratic tensor is reduced to 25 by noting that $B_{ij}^{\alpha\beta\gamma\delta}=B_{ij}^{\gamma\beta\alpha\delta}=B_{ij}^{\alpha\delta\gamma\beta}=B_{ij}^{\gamma\delta\alpha\beta}$ and that excluding terms which are independent of the spin orientation requires $\sum_{\alpha}B_{ij}^{\alpha\beta\alpha\delta}=\sum_{\beta}B_{ij}^{\alpha\beta\gamma\beta}=0$. The same conclusion as to the number of independent parameters can be arrived at via the spin cluster expansion of the magnetic energy [52, 53]

(see appendix D). Making use of the prototypical diagrams, we already recovered the isotropic biquadratic interaction $B_{ij}(\mathbf{S}_i \cdot \mathbf{S}_j)^2$ (1 parameter), and we uncovered the CBI given by $\mathbf{C}_{ij} \cdot (\mathbf{S}_i \times \mathbf{S}_j)(\mathbf{S}_i \cdot \mathbf{S}_j)$ (3 parameters). Considering prototypical diagrams with more spin–orbit sites is a constructive approach to populate the rest of the $B_{ij}^{\alpha\beta\gamma\delta}$ tensor, from which the form of the magnetic interactions will also follow. If spin–orbit coupling is weak, we then also obtain a natural classification of the various magnetic interactions in powers of this small parameter. This would justify considering only the isotropic biquadratic and the CBI as the most important interactions among all biquadratic ones. We note that in the upcoming sections discussing the *ab initio* based simulations, we do not make any assumption concerning the strength of the spin–orbit coupling.

3.1.6. Connection to a micromagnetic model

Since micromagnetic models are often used to describe magnetic properties of materials, it is useful to find the micromagnetic form of the CBI. As derived in appendix E, the new term in the micromagnetic energy density reads:

$$\mathcal{E}^{\mathrm{CBI}}(\mathbf{r}) = \sum_{\alpha,\beta,\gamma} \mathcal{C}_{\alpha\beta\gamma} \cdot (\mathbf{S}(\mathbf{r}) \times \partial_\alpha \mathbf{S}(\mathbf{r}))(\partial_\beta \mathbf{S}(\mathbf{r})) \cdot (\partial_\gamma \mathbf{S}(\mathbf{r})). \tag{7}$$

The explicit indices pertain to spatial derivatives, while vector components are handled by the standard notation for dot and cross products. Interestingly, other forms of higher-order interactions have been previously proposed [54]. We note, however, that ours is distinct and motivated by the microscopic derivation.

3.2. Magnetic interactions of dimers on various surfaces

In order to quantify the properties and significance of the CBI in relation to the other magnetic interactions, we present a systematic study of a series of prototypical systems: magnetic dimers on several surfaces where spin–orbit effects are expected to be significant. To do so, we construct a complete magnetic model containing all relevant interactions up to four-spin couplings by defining a mapping from a set of self-consistent constrained DFT calculations, as explained in section 2 and appendix D. The parametrizations of the complete magnetic model for all considered systems are given in appendix F.

3.2.1. Simplified magnetic model

We focus on the following interactions: the isotropic bilinear interaction $J\ \mathbf{S}_1 \cdot \mathbf{S}_2$, the DMI $\mathbf{D} \cdot (\mathbf{S}_1 \times \mathbf{S}_2)$, the isotropic biquadratic interaction $B(\mathbf{S}_1 \cdot \mathbf{S}_2)^2$, and the CBI $\mathbf{C} \cdot (\mathbf{S}_1 \times \mathbf{S}_2)(\mathbf{S}_1 \cdot \mathbf{S}_2)$. These are defined in terms of the unit vectors $\mathbf{S}_i$ representing the orientation of the spin magnetic moment of the ith atom in the dimer. The axis of the dimer is chosen as the x-axis, while the normal to the surface is chosen as the z-axis, as shown in figure 2(a). Symmetry then restricts the DMI and CBI vectors to lie in the yz-plane for (111) and (0001) surfaces, illustrated in figure 2(b), or to lie along the y-axis for the (001) surface. In all cases the y-component is the dominant one (see appendix F). To understand the interplay between the different interactions, we consider the simplified model obtained from equation (6) by confining the magnetic moments to the xz-plane and keeping only the mentioned interactions:

$$E(\alpha) = J\cos\alpha + D_y \sin\alpha + B\cos^2\alpha + C_y \sin\alpha\cos\alpha. \tag{8}$$

Here $\alpha = \theta_2 - \theta_1$ is the opening angle between the two magnetic moments. The angle that minimizes the energy can be written as $\alpha_{\min} = \alpha_J + \Delta\alpha$, where $\alpha_J = 0^\circ$ if $J < 0$ (ferromagnetic) or 180° if $J > 0$ (antiferromagnetic), and $\Delta\alpha$ is the canting induced by the remaining magnetic interactions. The energy can then be expanded as

$$\begin{aligned} E(\alpha_{\min}) &\approx E(\alpha_J) - (\mathrm{sgn}(J)D_y - C_y)\Delta\alpha + (|J| - 2B)\frac{(\Delta\alpha)^2}{2} \\ \Rightarrow \Delta\alpha &= \frac{180^\circ}{\pi}\,\frac{\mathrm{sgn}(J)D_y - C_y}{|J| - 2B}, \end{aligned} \tag{9}$$

where the last line gives an approximation to the canting angle. The canting angles obtained from the full magnetic parametrization are reported in appendix F. The main additional ingredient is the magnetic anisotropy, which in most cases leads to a small correction to the canting angles unless its magnitude is comparable to the DMI.

3.2.2. Magnetic dimers on Pt(111)

We first compare the magnetic properties of five different homoatomic dimers on the Pt(111) surface, with the corresponding data collected in table 1. All dimers except Ni possess large spin magnetic moments, which depend very weakly on the various imposed magnetic structures. Comparing the CBI to the DMI, we see that the magnitude of C_y is around 20%–30% of the one of D_y, even reaching 60% for Ni. For most dimers, B is similar in magnitude to the CBI, and is even stronger than the DMI for Cr and Ni. According to J, which is the dominant interaction, Cr and Mn are antiferromagnetic, while Fe, Co and Ni are ferromagnetic. Considering only J and D_y leads to a canting of the magnetic structure given by $\Delta\alpha^{2s}$ in table 1, while considering also B and C_y we obtain

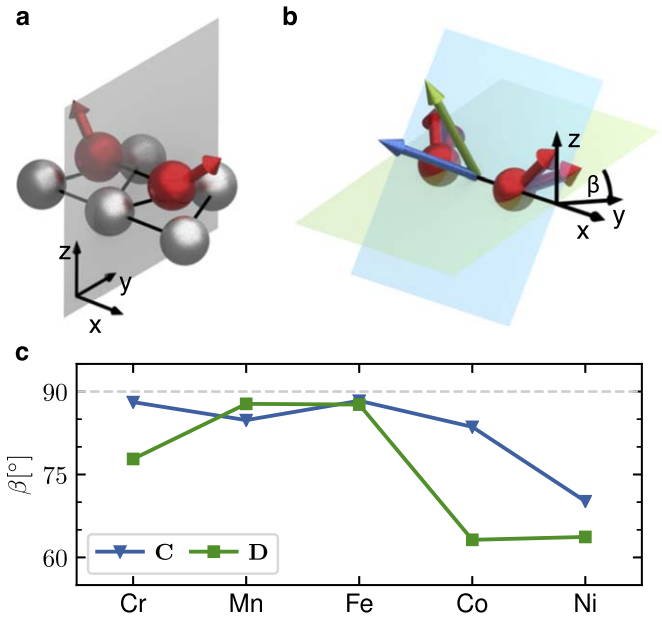

Figure 2. Illustration of the chiral interactions in a magnetic dimer. (a) Geometry: the dimer axis is along the *x*-direction, the surface normal defines the *z*-axis, and the mirror plane (gray) perpendicular to the bond is also shown. The atoms are represented by red spheres and their spin magnetic moments by solid arrows. Neighboring surface atoms are represented by gray spheres. (b) The CBI (blue) and DMI (green) vectors are shown as possibly noncollinear, and the dimer magnetic structures that they favor is also indicated. The plane containing the magnetic structure is characterized by its dihedral angle β with the *xy*-plane. (c) Dihedral angle β between the plane generated by the CBI or DMI vectors and the *xy*-plane for the Cr, Mn, Fe, Co and Ni dimers deposited on Pt(111).

Table 1. Spin moments, magnetic interaction parameters and opening angles of the magnetic ground state for Cr, Mn, Fe, Co and Ni dimers deposited on Pt(111). M is the spin magnetic moment of one atom in the dimer. The CBI and the DMI are represented by their dominant vector component C_y and D_y, respectively. The biquadratic and bilinear isotropic interactions are given by B and J, respectively. All interaction values are in meV. The canting angles are found by minimizing equation (8) with all the interactions ($\Delta\alpha^{4s}$) or keeping only J and D_y ($\Delta\alpha^{2s}$). The sign of $\Delta\alpha$represents the sign of $(\mathbf{S}_1 \times \mathbf{S}_2)_y$, the vector chirality of the magnetic ground state. For comparison, we also list the effective bilinear interactions defined by $D_y^{\mathrm{eff}} = D_y - \mathrm{sgn}(J)\,C_y$ and $J^{\mathrm{eff}} = \mathrm{J} - 2\,\mathrm{sgn}(J)B$.

Dimer		$M\,(\mu_B)$	C_y	D_y	B	J	$\Delta\alpha^{2s}$	$\Delta\alpha^{4s}$	D_y^{eff}	J^{eff}
Pt(111)	Cr	3.26	2.5	8.5	−11.7	35.8	−13°	−6°	6.0	59.2
	Mn	4.05	−0.6	−3.3	0.8	58.5	3°	3°	−2.7	56.9
	Fe	3.32	2.6	−7.3	−2.2	−43.0	10°	6°	−4.7	−47.4
	Co	2.12	−1.6	7.1	0.8	−76.8	−5°	−4°	5.5	−75.2
	Ni	0.62	0.5	0.8	−1.1	−5.4	−8°	−10°	1.3	−7.6
Pt(001)	Cr	2.53	2.5	11.2	−9.7	−35.3	−18°	−14°	13.7	−54.7
	Fe	3.24	−0.2	−9.5	−1.5	15.0	32°	28°	−9.3	12.0
Ir(111)	Cr	3.02	3.2	10.7	−12.1	29.5	−20°	−8°	7.5	53.7
	Fe	3.06	1.3	−14.6	−3.6	−16.3	42°	32°	−13.3	−23.3
Re(0001)	Cr	2.18	0.4	−18.1	−3.4	−16.4	48°	40°	−17.7	−23.2
	Fe	2.29	0.3	0.5	0.1	−2.3	−12°	−19°	0.8	−2.5

$\Delta\alpha^{4s}$. The difference between these values is the largest for Cr and Fe, so these are the dimers for which the biquadratic interactions are most important. Lastly, we also include the values of the effective bilinear interactions defined by the coefficients of $\Delta\alpha$ and $(\Delta\alpha)^2/2$ in equation (9). These correspond to $J^{\mathrm{eff}} = \mathrm{J} - 2\,\mathrm{sgn}(J)\,B$ and $D_y^{\mathrm{eff}} = D_y - \mathrm{sgn}(J)\,C_y$. The vector chirality of the magnetic ground state is set by the combination of the DMI and CBI vectors. These can be parallel, antiparallel, or substantially noncollinear (shown in figure 2(c)), in particular for the Co dimer. This shows that the CBI has not only the potential to impose the opposite vector spin chirality to the one favored by the DMI ($\Delta\alpha$ changing sign in equation (9)), but also to tilt in away from the direction defined by the DMI vector.

3.2.3. Cr and Fe dimers on other surfaces

The Cr and Fe dimers on Pt(111) were found to have the most important contributions from the CBI. To ascertain whether this is particular to the Pt(111) surface, we placed these dimers on other surfaces with strong

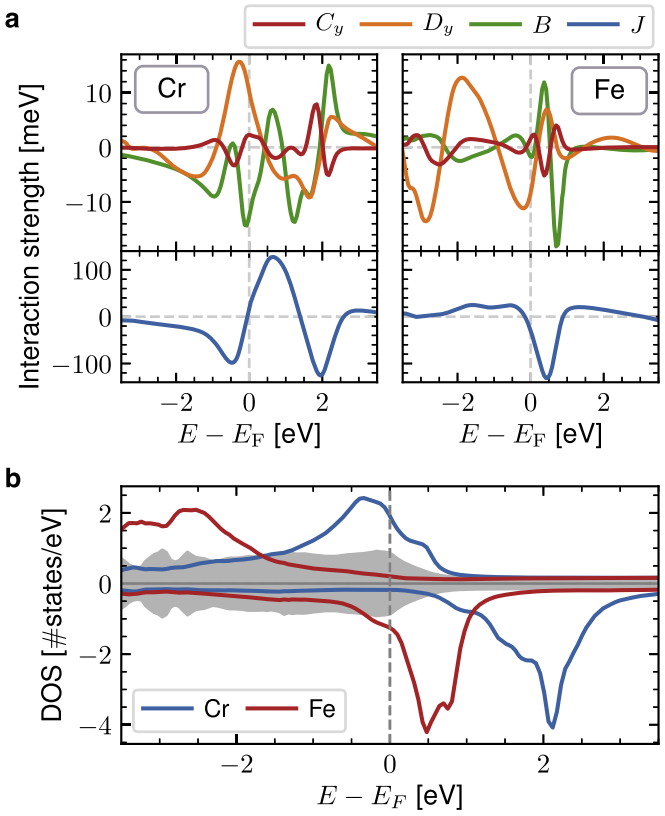

Figure 3. Relation between the magnetic interactions and the electronic structure of Cr and Fe dimers on Pt(111). (a) Energy dependence of the magnetic interactions in an energy window around the Fermi level for a Cr and an Fe dimer deposited on the Pt(111) surface. (b) Local density of states for an atom of the Cr and Fe dimers deposited on the Pt(111) surface. The local density of states of the Pt surface is shown as a gray background. The majority spin contribution is shown as positive and the minority as negative values.

spin–orbit coupling, namely Pt(001), Ir(111) and Re(0001). We see from table 1 that the CBI is generally a sizeable fraction of the DMI. On the Pt(001) and Ir(111) surfaces, the two dimers display a very large DMI, even comparable to the isotropic bilinear interaction J, leading to a strong canting of the magnetic structure. This canting is substantially modified when the biquadratic interactions are accounted for. The same behavior is found for the Cr dimer on Re(0001), while for the Fe dimer on this surface the interactions are found to be surprisingly weak, but still support a strongly noncollinear magnetic structure.

3.2.4. Electronic origin of the magnetic interactions

The origin of the different magnetic interactions can be further understood by comparing their dependence on the filling of the electronic states with the corresponding density of states of each dimer. This is shown in figure 3 for the Cr and Fe dimers on Pt(111). D_y is largest in the energy range of the Pt d-states, which shows that the DMI is strongly enhanced by hybridization of the magnetic d-states of the dimer with the d-states of the Pt surface. B and C_y (and also J) have their largest values in the small energy range of the minority d-states of the Fe dimer, which suggests that the biquadratic interactions require less hybridization with Pt and so more localized magnetic d-states in the dimer. This can be understood from the microscopic theory. According to the prototypical diagrams in figures 1(a), (c), the isotropic interactions are direct interactions between the dimer atoms, resulting in a strong dependence on the Fe d-states. The prototypical diagram of figure 1(b) shows that the DMI is an interaction mediated by a spin–orbit site, which are supplied by the Pt surface atoms, and so this interaction is strongly dependent on the Pt d-states. The CBI involves both a direct exchange between the magnetic sites and an excursion through a spin–orbit site, figure 1(d), so it can be amplified in those two ways, leading to a more complicated dependence.

3.3. Implications of the CBI

The CBI has different important implications for a broad class of noncollinear magnetic nanostructures. For a magnetic dimer, we already found that the CBI influences the opening angle and the vector spin chirality of the magnetic structure. To gain further understanding, we return to the previous example of a CBI vector in the y-direction, for which the interaction energy has the form $E_{\mathrm{CBI}}(\alpha) = C_y \sin\alpha \cos\alpha$ (see equation (8)). The $\cos\alpha$ term comes from the $\mathbf{S}_1 \cdot \mathbf{S}_2$ part of the interaction, while the $\sin\alpha$ terms comes from $(\mathbf{S}_1 \times \mathbf{S}_2)_y$, with α the

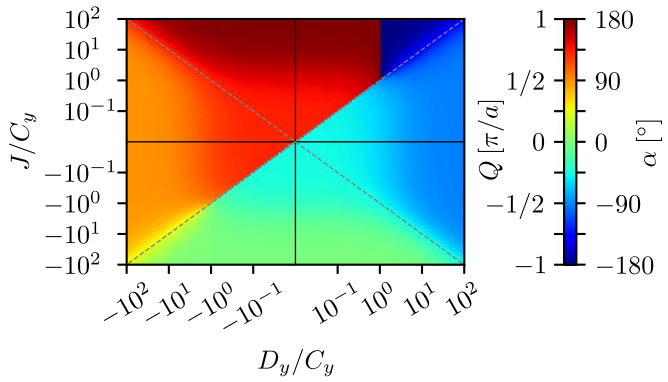

Figure 4. Magnetic ground states of a dimer and of an infinite chain stabilized by the isotropic bilinear interaction J, the DMI D_y and the CBI C_y. The magnetic ground state is characterized by the opening angle α between two neighboring magnetic moments, obtained by minimizing equation (8), which for an infinite chain defines a spin spiral with wavevector $Q = \alpha/a$ (a being the nearest-neighbor distance). C_y is chosen to be positive.

opening angle. As the dot product is isotropic, the opening is favored in the plane perpendicular to the CBI vector. Fixing $C_y > 0$ for definiteness, there are two energy minima for $\alpha_{\min} \in \{-45°,\ 135°\}$, and two maxima for $\alpha_{\max} \in \{45°,\ -135°\}$. Strikingly, the two values of $\alpha_{\min}$ have opposite signs, which means that the sign of their vector spin chirality (projected on the y-axis) is also opposite. Thus, and in contrast to the DMI, the CBI favors both possible rotational senses at once (although with different opening angles). In other words, the CBI is not chiral on its own, but supports a definite chirality in the presence of other interactions. This is irrespective of whether those interactions are chiral, such as DMI, or not, such as the bilinear isotropic exchange. Starting from a ferromagnetic or antiferromagnetic structure (set by J), the DMI will induce a canting of the same rotational sense for both cases, while the CBI will favor cantings for each structure which have opposite rotational senses.

3.3.1. From a dimer to an infinite chain

Next we relate the magnetic ground state of a dimer to that of an infinite chain, assuming that the interactions present are J, D_y and C_y being nearest-neighbor interactions for the chain. We take $B = 0$ for simplicity, as typically $|B| \ll |J|$ and so it makes a small correction to the opening angle, see equation (9). The energy as a function of the opening angle for the dimer is given by equation (8), and the same form applies for the energy of a spiral magnetic structure on an infinite chain, with $\mathbf{S}_i = \sin(Qx_i)\mathbf{S}_x + \cos(Qx_i)\mathbf{S}_z$, by setting $Q = \alpha/a$ (a is the nearest-neighbor distance). The canting angle/spiral wavevector that minimizes the energy is shown for different values of D_y/C_y and J/C_y in figure 4. The sharp transition in the sign of α found along $J = D_y$ is driven by C_y, and signals a change in the sign of the vector spin chirality. At the edges of the diagram we recover well-known magnetic structures ($\alpha = 0°,\ 180°$ are the ferromagnetic and antiferromagnetic structures for J-only, respectively, and $\alpha = \pm 90°$ pertain to D_y-only).

3.3.2. Impact of the CBI on complex 2D magnetic structures

As a final example, we consider two-dimensional magnetic systems. Since higher-order isotropic interactions can help stabilizing complex magnetic structures called multiple-Q-states [20–22, 38], we address the potential role of the CBI, choosing the Fe monolayer on Ir(111) by way of example [38]. The ground state is a nanoskyrmion lattice, which is a type of 2Q-state made of two symmetry-related wavevectors $\mathbf{Q}_1$ and $\mathbf{Q}_2$. Other combinations lead to further noncollinear states which were calculated to have a similar energy: single-Q spin spirals, the $\mathbf{Q}_m$-star and $\mathbf{Q}_m$-vortex states, and the nanovortex lattice. These magnetic structures are visualized in figures 5(a)–(f), with the triangular Néel state included for comparison. To show how different magnetic interactions affect these states, we write each energy contribution as $E_I = NI\Gamma_I$, where N is the number of atoms in the magnetic unit cell, $I = \{D, B, C\}$ is the interaction strength, and Γ_I is a factor determined by the lattice and the magnetic structure.

This factor encodes either the relative angles between the magnetic moments (for the isotropic biquadratic interaction) or the alignment of the vector chiralities with the directions defined by the DMI and CBI. Since our goal is to identify which magnetic states are favored or unfavoured by each interaction, the actual interaction strength I is not relevant. Figure 5(g) plots the Γ_I factors computed assuming nearest-neighbor pair interactions following C_{3v} symmetry. We do not discuss the contribution of J, as this interaction is complex and long-ranged for this system [38]. Interestingly, the contribution of the isotropic biquadratic interaction B is similar for every structure, none being particularly favored. On the other hand, both the DMI as well as the CBI do favor certain magnetic structures. The DMI favors almost equally the single-Q spiral and the nanoskyrmion lattice, while the CBI clearly favors the

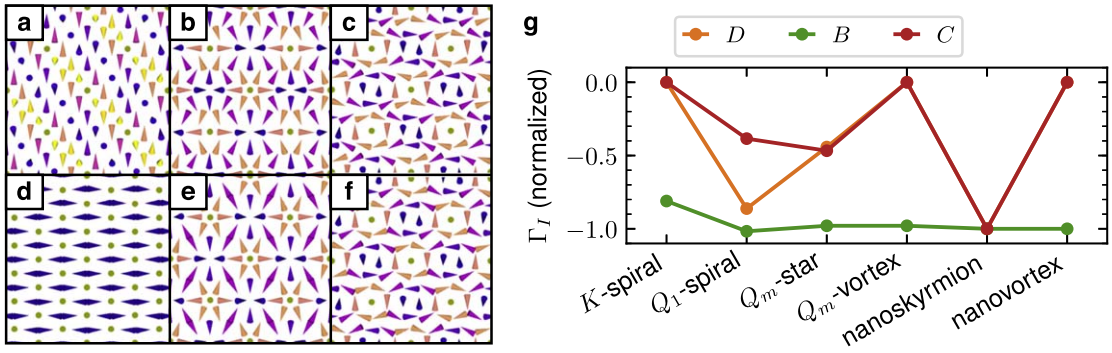

Figure 5. Contributions from different magnetic interactions to the energy of various magnetic structures. The considered magnetic structures are: single-Q spin spirals for the (a) Q_1-vector and (d) and for the K-vector (Néel state); the 2Q-states (b) Q_m-star and (c) Q_m-vortex; and the two noncollinear states forming (e) a nanoskyrmion lattice and (f) a nanovortex lattice. (g) The Γ_I factors describe how the contribution to the energy from different interactions varies among the several magnetic structures (see main text for discussion). The considered interactions are the DMI D, the isotropic biquadratic interaction B and the CBI C. The factors are normalized with respect to the nanoskyrmion lattice. These magnetic structures were discussed in connection to the magnetic ground state of an Fe monolayer on Ir(111) in [38].

nanoskyrmion lattice (2Q state) over the spin spirals. This shows that the CBI can play a deciding role in stabilizing noncoplanar multiple-Q-states, which have a non-vanishing scalar spin chirality.

4. Discussion

We presented a comprehensive analysis of a new chiral higher-order magnetic pair interaction, the CBI. Beside providing its atomistic form we derived its expression in the micromagnetic limit. Using a microscopic model and a systematic expansion of the electronic grand-potential, we identified the prototypical diagrams behind all kinds of magnetic interactions. This led us to uncover a new chiral interaction, the CBI, which is linear in the spin–orbit coupling and is the biquadratic equivalent of the DMI, following the same symmetry rules obeyed by the latter interaction. In its most general form, this interaction couples four distinct magnetic sites, and consists of terms of the form $\mathbf{C}_{ijkl} \cdot (\mathbf{S}_i \times \mathbf{S}_j)(\mathbf{S}_k \cdot \mathbf{S}_l)$. In micromagnetic form, it becomes $\sum_{\alpha,\beta,\gamma} \boldsymbol{\mathcal{C}}_{\alpha\beta\gamma} \cdot (\mathbf{S}(\mathbf{r}) \times \partial_\alpha \mathbf{S}(\mathbf{r}))(\partial_\beta \mathbf{S}(\mathbf{r}) \cdot \partial_\gamma \mathbf{S}(\mathbf{r}))$. We note that two recent studies have found signatures of higher-order interactions in magnetic chains on the Re(0001) surface [55] and in bulk MnGe [56]. We proved the existence and quantified the importance of this new interaction in relation to other well-known ones by performing systematic first-principles calculations for prototypical systems, magnetic dimers on surfaces with strong spin–orbit coupling. For these dimers, the CBI is typically around 20%–30% of the DMI, reaching 60% for a Ni dimer deposited on Pt(111). Furthermore, we contrasted the properties of the CBI with those of the DMI, revealing that the CBI can simultaneously favor structures with opposite vector spin chiralities (canted ferromagnetic versus canted antiferromagnetic structure), and that the CBI vector is not necessarily parallel to the DMI one. Insight into the electronic origin of the CBI and the other magnetic interactions was obtained via their dependence on the filling of the electronic states, supporting the proposed mechanism derived from the microscopic model. We related the magnetic phase diagram of a dimer to that of an infinite chain, and surveyed the implications of the CBI for magnetic monolayers. Considering several magnetic structures relevant for an Fe monolayer on Ir(111), we showed that the CBI can play a deciding role in favoring a noncoplanar nanoskyrmion lattice over other possible structures. We thus conclude that the CBI can influence simultaneously the vector and the scalar spin chirality, opening new avenues for stabilizing and engineering complex magnetic textures with both fundamental and technological interest. We also expect that there should be a non-trivial impact on the related dynamics, transport and topological properties, which should motivate future investigations.

Acknowledgments

This work was supported by the European Research Council (ERC) under the European Union's Horizon 2020 research and innovation program (ERC-consolidator grant 681405—DYNASORE). The authors gratefully acknowledge the computing time granted through JARA-HPC on the supercomputer JURECA at the Forschungszentrum Jülich [49].

Appendix A. Structural relaxations

The structural relaxations are performed using the density functional theory package Quantum Espresso [46]. Exchange and correlation effects are treated in the generalized gradient approximation using the PBEsol

Table A1. Relaxations of the adatoms towards the surfaces relative to the interlayer distances obtained from Quantum Espresso calculations. Shown are the reduction r of the mean vertical distance d between the adatom and the first surface layer, according to $d = (1 - r)\,d_0$, d_0 being the bulk interlayer distance. No value is provided when Ni was found to be nonmagnetic at its equilibrium geometry. The last column lists the relaxations used to set up the geometry for the KKR calculations. When multiple values are given, the one which is closest to the QE result was used for the corresponding element.

	Cr	Mn	Fe	Co	Ni	KKR geometry
Pt(111)	19.4%	17.9%	25.9%	27.5%	25.2%	20%
Pt(001)	34.4%	33.3%	32.2%	30.4%	—	30%
Ir(111)	11.5%	11.7%	17.9%	20.6%	—	15%
Re(0001)	16.1%	12.7%	18.6%	21.8%	—	15/20%

functional [48] with ultrasoft pseudopotentials in the scalar relativistic approximation [47]. The different surfaces are modeled by a 4×4 supercell with 5 layers and a vacuum region corresponding to 5 interlayer distances using $2 \times 2 \times 1$ k-points in the Monkhorst–Packgrid. The theoretical lattice constants were obtained from bulk calculations with a $8 \times 8 \times 8$ k-point mesh. Test calculations showed that the dimers have similar structural relaxations to those of the adatoms, so for simplicity we considered the latter. The different adatoms are placed in the threefold hollow positions on the hexagonal surfaces—fcc-like for Pt(111) and Ir(111) and hcp-like for Re(0001)—, and on the fourfold hollow position for Pt(001). The adatom as well as the atoms in the first surface layer are allowed to relax. Table A1 shows the obtained relaxations towards the surfaces for the different adatoms on the different surfaces in terms of the bulk inter-layer distances and the relaxations which are used to set up the geometry for the KKR-based calculations.

Appendix B. Diagrammatic expansion of the grand potential

Starting from $\sigma^\alpha\sigma^\beta = \delta_{\alpha\beta}\sigma^0 + \mathrm{i}\epsilon_{\alpha\beta\gamma}\sigma^\gamma$, we obtain useful relations from which all possible forms of the magnetic interactions can be extracted:

$$\frac{1}{2}\,\mathrm{Tr}\;\sigma^\alpha\sigma^\beta = \delta_{\alpha\beta}, \tag{B.1}$$

$$\frac{1}{2}\,\mathrm{Tr}\;\sigma^\alpha\sigma^\beta\sigma^\gamma = \mathrm{i}\;\epsilon_{\alpha\beta\gamma}, \tag{B.2}$$

$$\frac{1}{2}\,\mathrm{Tr}\;\sigma^\alpha\sigma^\beta\sigma^\gamma\sigma^\delta = \delta_{\alpha\beta}\delta_{\gamma\delta} - \delta_{\alpha\gamma}\delta_{\beta\delta} + \delta_{\beta\gamma}\delta_{\alpha\delta}, \tag{B.3}$$

$$\frac{1}{2}\,\mathrm{Tr}\;\sigma^\alpha\sigma^\beta\sigma^\gamma\sigma^\delta\sigma^\eta = \mathrm{i}(\delta_{\delta\eta}\epsilon_{\alpha\beta\gamma} + \delta_{\alpha\beta}\epsilon_{\gamma\delta\eta} + \delta_{\alpha\gamma}\epsilon_{\beta\delta\eta} + \delta_{\beta\gamma}\epsilon_{\alpha\delta\eta}), \tag{B.4}$$

$$\begin{aligned}\frac{1}{2}\,\mathrm{Tr}\;\sigma^\alpha\sigma^\beta\sigma^\gamma\sigma^\delta\sigma^\eta\sigma^\zeta = {}& \delta_{\alpha\beta}\delta_{\gamma\delta}\delta_{\eta\zeta} - \delta_{\alpha\gamma}\delta_{\beta\delta}\delta_{\eta\zeta} + \delta_{\beta\gamma}\delta_{\alpha\delta}\delta_{\eta\zeta} - \epsilon_{\alpha\beta\gamma}\epsilon_{\delta\eta\zeta} - \delta_{\alpha\beta}\delta_{\gamma\eta}\delta_{\delta\zeta},\\ & + \delta_{\alpha\beta}\delta_{\delta\eta}\delta_{\gamma\zeta} - \delta_{\alpha\gamma}\delta_{\beta\eta}\delta_{\delta\zeta} + \delta_{\alpha\gamma}\delta_{\delta\eta}\delta_{\beta\zeta} - \delta_{\beta\gamma}\delta_{\alpha\eta}\delta_{\delta\zeta} + \delta_{\beta\gamma}\delta_{\delta\eta}\delta_{\alpha\zeta}.\end{aligned} \tag{B.5}$$

In the following derivations, two different Green functions will be employed, according to the following partition of the electronic hamiltonian (the parts will be specified later):

$$\mathcal{H} = \mathcal{H}^0 + \Delta\mathcal{H} \quad \Rightarrow \quad G(E) = (E - \mathcal{H})^{-1}, \quad G^0(E) = (E - \mathcal{H}^0)^{-1}. \tag{B.6}$$

For a given energy E, the two Green functions are connected by the Dyson equation

$$G(E) = G^0(E) + G^0(E)\Delta\mathcal{H}\,G(E). \tag{B.7}$$

The electronic grand potential Ω is given by

$$\Omega = -\frac{1}{\beta}\int_{-\infty}^{\infty} \mathrm{d}E\,\ln(1 + \mathrm{e}^{\beta(\mu - E)})\int \mathrm{d}\mathbf{r}\;\mathrm{Tr}\;\rho(\mathbf{r}, \mathbf{r}; E). \tag{B.8}$$

Here $\beta = 1/k_\mathrm{B}T$ with k_B the Boltzmann constant and T the temperature, and μ is the chemical potential. The position integral is over the whole volume of the system, and the trace is over the spin components. The spectral density matrix $\rho(\mathbf{r}, \mathbf{r}'; E)$ is a 2×2 matrix in spin space, and can be expressed in terms of the single-particle Green function by

$$\rho(\mathbf{r}, \mathbf{r}'; E) = -\frac{1}{\pi}\,\mathrm{Im}\;G(\mathbf{r}, \mathbf{r}'; E) = \frac{G(\mathbf{r}, \mathbf{r}'; E - \mathrm{i}0) - G(\mathbf{r}, \mathbf{r}'; E + \mathrm{i}0)}{2\pi\mathrm{i}}. \tag{B.9}$$

For simplicity, the spatial dependence is omitted in the following. By recursively inserting the Dyson equation, equation (B.7), into the expression for Ω we find

$$\Omega = -\frac{1}{\beta}\,\mathrm{Im}\int_{-\infty}^{\infty} \mathrm{d}E\,\ln(1+e^{\beta(\mu-E)})\,\mathrm{Tr}\left(G^0(E)+G^0(E)\sum_{p=1}^{\infty}[\Delta\mathcal{H}\,G^0(E)]^p\right)$$
$$= \Omega^0 + \sum_{p=1}^{\infty}\Omega^p. \tag{B.10}$$

This is a formal power series that can be used to develop a diagrammatic expansion of the grand potential. Using the relation

$$\mathrm{Tr}\;G^0(E)[\Delta\mathcal{H}\,G^0(E)]^p = -\frac{1}{p}\frac{\partial}{\partial E}\,\mathrm{Tr}\;[\Delta\mathcal{H}\,G^0(E)]^p \tag{B.11}$$

and integrating by parts with respect to the energy, we find

$$\Omega^p = -\frac{1}{\pi}\,\mathrm{Im}\int_{-\infty}^{\infty}\mathrm{d}E\,f(E;\,\mu)\frac{1}{p}\,\mathrm{Tr}\;[\Delta\mathcal{H}\,G^0(E)]^p, \tag{B.12}$$

where $f(E;\mu)$ is the Fermi distribution function. If one inserts the spectral representation of the Green function,

$$G^0(E) = \sum_{\lambda}\frac{|\lambda\rangle\langle\lambda|}{E-E_\lambda}, \tag{B.13}$$

it is straightforward to verify that the formal power series corresponds to infinite-order perturbation theory, regarding $\mathcal{H}^0$ as the unperturbed system and $\Delta\mathcal{H}$ as the perturbation.

The electronic hamiltonian can be written as the sum of three parts,

$$\mathcal{H} = \mathcal{H}^0 + \mathcal{H}^{\mathrm{mag}} + \mathcal{H}^{\mathrm{soc}}. \tag{B.14}$$

For illustration purposes, these terms will be represented using real Wannier-like basis functions. The non-spin-dependent terms are collected into

$$\mathcal{H}^0 = \sum_{m,n}\sum_{\mu,\nu}\sum_{s} c^{\dagger}_{m\mu s}\,t_{m\mu,n\nu}\,c_{n\nu s}, \tag{B.15}$$

where the atomic sites are labeled by m and n, the orbital character of the Wannier-like basis functions by μ and ν, and the spin components by s. Here $c^{\dagger}$ and c are creation and annihilation operators for electrons in the Wannier-like basis. The magnetic part of the hamiltonian is taken to be of the form

$$\mathcal{H}^{\mathrm{mag}} = \sum_{i}\mathcal{H}^{\mathrm{mag}}_i, \tag{B.16}$$

$$\mathcal{H}^{\mathrm{mag}}_i = \sum_{\mu,\nu}\sum_{s,s'} c^{\dagger}_{i\mu s}\,U_{i\mu\nu}\,\mathbf{S}_i\cdot\boldsymbol{\sigma}_{ss'}\,c_{i\nu s'}. \tag{B.17}$$

The magnetic sites are labeled $m = i, j, \ldots$ to be distinguishable from other non-magnetic or spin–orbit sites, with $\mathbf{S}_i$ the orientation of the magnetic moment on site i. The final term is the atomic spin–orbit coupling,

$$\mathcal{H}^{\mathrm{soc}} = \sum_{a}\mathcal{H}^{\mathrm{soc}}_a, \tag{B.18}$$

$$\mathcal{H}^{\mathrm{soc}}_a = \sum_{\mu,\nu}\sum_{s,s'} c^{\dagger}_{a\mu s}\,\lambda_a\,\mathbf{L}_{\mu\nu}\cdot\boldsymbol{\sigma}_{ss'}\,c_{a\nu s'}, \tag{B.19}$$

with the local orbital angular momentum operator $\mathbf{L}$. As done for the magnetic sites, we label the spin–orbit sites by a different variable, $m = a, b, \ldots$. We have that $t_{m\mu,n\nu} = t_{n\nu,m\mu}$, $U_{i\mu\nu} = U_{i\nu\mu}$ and $\mathbf{L}_{\mu\nu} = -\mathbf{L}_{\nu\mu}$, assuming that the angular part of the Wannier-like basis functions correspond to real spherical harmonics centered on each site.

Returning to the formal power series for the electronic grand potential, we now identify $\Delta\mathcal{H} = \mathcal{H}^{\mathrm{mag}} + \mathcal{H}^{\mathrm{soc}}$, so that we have a double expansion in magnetic and spin–orbit terms It follows that Ω^p can be further split into contributions $\Omega^{p,k}$ which contain $\mathcal{H}^{\mathrm{mag}}$ k-times and $\mathcal{H}^{\mathrm{soc}}$ (p–k)-times, for all $k = 0, 1, \ldots, p$. We wish to construct an effective magnetic model by taking the orientations of the magnetic moments $\mathbf{S}_i$ as independent variables. From the basic requirement of time-reversal invariance of the magnetic energy, only the contributions $\Omega^{p,k}$ for which k is an even number (i.e. we have an even number of $\mathbf{S}_i$'s in the final expression) should be give a finite contribution. We can then write

$$\Omega = \Omega^0 + \Omega^{\mathrm{soc}} + \sum_{p}\sum_{k=1}^{p/2}\Omega^{p,2k}[\{\mathbf{S}\}], \tag{B.20}$$

where all contributions arising solely from spin–orbit ($k = 0$) are collected in Ω^{soc}.

The $p = 2k$ terms generate all possible isotropic magnetic interactions. The $p = 2$ term is (no restrictions on the sum)

$$\Omega^{2,2} = \frac{1}{2}\sum_{i,j}\Omega_{ij}^{2,2}, \tag{B.21}$$

which leads to the isotropic bilinear interaction (2-spin 2-site)

$$\begin{aligned}\Omega_{ij}^{2,2} &= -\frac{1}{\pi}\,\mathrm{Im}\int_{-\infty}^{\infty}\mathrm{d}E\, f(E;\,\mu)\mathrm{Tr}\;\mathcal{H}_i^{\mathrm{mag}}G_{ij}^0(E)\mathcal{H}_j^{\mathrm{mag}}G_{ji}^0(E)\\ &= -\frac{1}{\pi}\,\mathrm{Im}\int_{-\infty}^{\infty}\mathrm{d}E\, f(E;\,\mu)\mathrm{Tr}\;U_iG_{ij}^0(E)U_jG_{ji}^0(E)(\mathbf{S}_i\cdot\mathbf{S}_j\,\sigma_0+\mathrm{i}(\mathbf{S}_i\times\mathbf{S}_j)\cdot\boldsymbol{\sigma})\\ &= J_{ij}^{2,2}\,\mathbf{S}_i\cdot\mathbf{S}_j,\end{aligned} \tag{B.22}$$

by considering the trace over spin indices. The $i = j$ part corresponds to a contribution to the energy from the local exchange splitting. The $p = 4$ term is

$$\Omega^{4,4} = \frac{1}{4}\sum_{i,j,k,l}\Omega_{ijkl}^{4,4}, \tag{B.23}$$

where

$$\begin{aligned}\Omega_{ijkl}^{4,4} &= -\frac{1}{\pi}\,\mathrm{Im}\int_{-\infty}^{\infty}\mathrm{d}E\, f(E;\,\mu)\mathrm{Tr}\;\mathcal{H}_i^{\mathrm{mag}}G_{ij}^0(E)\mathcal{H}_j^{\mathrm{mag}}G_{jk}^0(E)\mathcal{H}_k^{\mathrm{mag}}G_{kl}^0(E)\mathcal{H}_l^{\mathrm{mag}}G_{li}^0(E)\\ &= J_{ijkl}^{4,4}((\mathbf{S}_i\cdot\mathbf{S}_j)(\mathbf{S}_k\cdot\mathbf{S}_l)-(\mathbf{S}_i\cdot\mathbf{S}_k)(\mathbf{S}_j\cdot\mathbf{S}_l)+(\mathbf{S}_i\cdot\mathbf{S}_l)(\mathbf{S}_j\cdot\mathbf{S}_k)).\end{aligned} \tag{B.24}$$

Thus $\Omega_{iikk}^{4,4}$ does not depend on the magnetic orientations, $\Omega_{iikl}^{4,4}\propto\mathbf{S}_k\cdot\mathbf{S}_l$ contributes to the isotropic bilinear interaction (2-spin 2-site), $\Omega_{ijij}^{4,4}\propto 2(\mathbf{S}_i\cdot\mathbf{S}_j)^2-1$ contributes to the isotropic biquadratic interaction (4-spin 2-site), $\Omega_{ijil}^{4,4}\propto 2(\mathbf{S}_i\cdot\mathbf{S}_j)(\mathbf{S}_i\cdot\mathbf{S}_l)-\mathbf{S}_j\cdot\mathbf{S}_l$ gives an isotropic 4-spin 3-site interaction and a correction to the bilinear one, and $\Omega_{ijkl}^{4,4}$ is the general form of the isotropic 4-spin 4-site interaction. It is clear from all these examples that terms that contain the same magnetic site consecutively (e.g. *iikk* or *iikl* in the previous expression) will not lead to new forms of the magnetic interaction than simpler expressions (e.g. $\Omega_{ij}^{2,2}$), so they can be excluded from the search for new forms of the magnetic interaction.

Next, consider the terms that contain both $\mathcal{H}^{\mathrm{mag}}$ and $\mathcal{H}^{\mathrm{soc}}$. The lowest-order term is

$$\Omega^{3,2} = \frac{1}{3}\sum_{i,j}\Omega_{ij}^{3,2}, \tag{B.25}$$

and gives the first contribution to the bilinear DMI,

$$\begin{aligned}\Omega_{ij}^{3,2} &= -\frac{1}{\pi}\,\mathrm{Im}\int_{-\infty}^{\infty}\mathrm{d}E\, f(E;\,\mu)3\sum_a\mathrm{Tr}\;\mathcal{H}_i^{\mathrm{mag}}G_{ij}^0(E)\mathcal{H}_j^{\mathrm{mag}}G_{ja}^0(E)\mathcal{H}_a^{\mathrm{soc}}G_{ai}^0(E)\\ &= -\frac{1}{\pi}\,\mathrm{Im}\int_{-\infty}^{\infty}\mathrm{d}E\, f(E;\,\mu)6\sum_a\mathrm{i}\;\mathrm{Tr}\;G_{ai}^0(E)U_iG_{ij}^0(E)U_jG_{ja}^0(E)\lambda_a\,\mathbf{L}\cdot(\mathbf{S}_i\times\mathbf{S}_j)\\ &= \frac{3}{2}\sum_a\mathbf{D}_{ij,a}^{3,2}\cdot(\mathbf{S}_i\times\mathbf{S}_j) = \frac{3}{2}\,\mathbf{D}_{ij}^{3,2}\cdot(\mathbf{S}_i\times\mathbf{S}_j).\end{aligned} \tag{B.26}$$

The factor of 3 on the first line is due to the three different places where $\mathcal{H}^{\mathrm{soc}}$ can be inserted, which are all equivalent due to the cyclic properties of the trace. On the second line the factor of 6 is a result of the spin trace, with the remaining trace being over the orbital indices. The final prefactor of $3/2$ is for consistency with the overall total prefactor of $1/2$ for the 2-site magnetic interactions. The DMI vector is then given explicitly as a sum of contributions arising from different spin–orbit sites, in analogy to the model of Lévy and Fert.

The next contribution to the bilinear interactions is given by

$$\Omega^{4,2} = \frac{1}{4}\sum_{i,j}\Omega_{ij}^{4,2}. \tag{B.27}$$

There are six ways of combining $\mathcal{H}^{\mathrm{mag}}$ and $\mathcal{H}^{\mathrm{soc}}$ for this, which can be grouped into two contributions by exploiting the cyclic property of the trace. We find

$$\Omega_{ij}^{4,2} = -\frac{1}{\pi}\,\mathrm{Im}\int_{-\infty}^{\infty} \mathrm{d}E\, f(E;\,\mu) 4 \sum_{a,b} \mathrm{Tr}\; \mathcal{H}_i^{\mathrm{mag}} G_{ij}^0(E) \mathcal{H}_j^{\mathrm{mag}} G_{ja}^0(E) \mathcal{H}_a^{\mathrm{soc}} G_{ab}^0(E) \mathcal{H}_b^{\mathrm{soc}} G_{bi}^0(E)$$
$$- \frac{1}{\pi}\,\mathrm{Im}\int_{-\infty}^{\infty} \mathrm{d}E\, f(E;\,\mu) 2 \sum_{a,b} \mathrm{Tr}\; \mathcal{H}_i^{\mathrm{mag}} G_{ia}^0(E) \mathcal{H}_a^{\mathrm{soc}} G_{ja}^0(E) \mathcal{H}_j^{\mathrm{mag}} G_{jb}^0(E) \mathcal{H}_b^{\mathrm{soc}} G_{bi}^0(E)$$
$$= 2(J_{ij}^{4,2}\,\mathbf{S}_i \cdot \mathbf{S}_j + \mathbf{S}_i \cdot D_{ij}^{4,2} \cdot \mathbf{S}_j + \mathbf{S}_i \cdot A_{ij}^{4,2} \cdot \mathbf{S}_j). \tag{B.28}$$

There is a contribution to the isotropic bilinear interaction

$$J_{ij}^{4,2} = -\frac{1}{\pi}\,\mathrm{Im}\int_{-\infty}^{\infty} \mathrm{d}E\, f(E;\,\mu) 4 \sum_{a,b} \sum_{\alpha} \mathrm{Tr}\; U_i G_{ij}^0(E) U_j G_{ja}^0(E) \lambda_a L^\alpha G_{ab}^0(E) \lambda_b L^\alpha G_{bi}^0(E)$$
$$+ \frac{1}{\pi}\,\mathrm{Im}\int_{-\infty}^{\infty} \mathrm{d}E\, f(E;\,\mu) 2 \sum_{a,b} \sum_{\alpha} \mathrm{Tr}\; U_i G_{ia}^0(E) \lambda_a L^\alpha G_{aj}^0(E) U_j G_{jb}^0(E) \lambda_b L^\alpha G_{bi}^0(E), \tag{B.29}$$

and another contribution to the DMI (in matrix form, with $\alpha = x, y, z$)

$$D_{ij}^{4,2,\alpha\beta} = \frac{1}{\pi}\,\mathrm{Im}\int_{-\infty}^{\infty} \mathrm{d}E\, f(E;\,\mu) 4 \sum_{a,b} \mathrm{Tr}\; U_i G_{ij}^0(E) U_j G_{ja}^0(E) \lambda_a L^\alpha c \lambda_b L^\beta G_{bi}^0(E)$$
$$- \frac{1}{\pi}\,\mathrm{Im}\int_{-\infty}^{\infty} \mathrm{d}E\, f(E;\,\mu) 4 \sum_{a,b} \mathrm{Tr}\; U_i G_{ij}^0(E) U_j G_{ja}^0(E) \lambda_a L^\beta G_{ab}^0(E) \lambda_b L^\alpha G_{bi}^0(E). \tag{B.30}$$

The first contribution to the anisotropic symmetric bilinear interaction is given by

$$A_{ij}^{4,2,\alpha\beta} = -\frac{1}{\pi}\,\mathrm{Im}\int_{-\infty}^{\infty} \mathrm{d}E\, f(E;\,\mu) 2 \sum_{a,b} \mathrm{Tr}\; U_i G_{ia}^0(E) \lambda_a L^\alpha G_{aj}^0(E) U_j G_{jb}^0(E) \lambda_b L^\beta G_{bi}^0(E)$$
$$- \frac{1}{\pi}\,\mathrm{Im}\int_{-\infty}^{\infty} \mathrm{d}E\, f(E;\,\mu) 2 \sum_{a,b} \mathrm{Tr}\; U_i G_{ia}^0(E) \lambda_a L^\beta G_{aj}^0(E) U_j G_{jb}^0(E) \lambda_b L^\alpha G_{bi}^0(E), \tag{B.31}$$

and arises when the two magnetic sites are connected through a spin–orbit site. In the case of $i = j$ it becomes a contribution to the on-site magnetic anisotropy. We see that the terms containing $G_{ab}^0(E)$, i.e. consecutive scattering from two spin–orbit sites, generate corrections to the interactions found already at lower orders in the expansion, so they can be excluded from the search for new forms of the magnetic interaction. The new kind of interaction found at this order is the anisotropic symmetric bilinear interaction.

The first kind of anisotropic higher-order interaction arises from

$$\Omega^{5,4} = \frac{1}{5} \sum_{i,j,k,l} \Omega_{ijkl}^{5,4}. \tag{B.32}$$

It generates a DMI-like 4-spin 4-site interaction:

$$\Omega_{ijkl}^{5,4} = -\frac{1}{\pi}\,\mathrm{Im}\int_{-\infty}^{\infty} \mathrm{d}E\, f(E;\,\mu)$$
$$\times 5 \sum_{a} \mathrm{Tr}\; \mathcal{H}_i^{\mathrm{mag}} G_{ij}^0(E) \mathcal{H}_j^{\mathrm{mag}} G_{jk}^0(E) \mathcal{H}_k^{\mathrm{mag}} G_{kl}^0(E) \mathcal{H}_l^{\mathrm{mag}} G_{la}^0(E) \mathcal{H}_a^{\mathrm{soc}} G_{ai}^0(E)$$
$$= \frac{5}{4}\,\mathbf{C}_{ijkl}^{5,4} \cdot ((\mathbf{S}_i \cdot \mathbf{S}_j)\mathbf{S}_k \times \mathbf{S}_l - (\mathbf{S}_i \cdot \mathbf{S}_k)\mathbf{S}_j \times \mathbf{S}_l + (\mathbf{S}_i \cdot \mathbf{S}_l)\mathbf{S}_j \times \mathbf{S}_k$$
$$+ (\mathbf{S}_j \cdot \mathbf{S}_k)\mathbf{S}_i \times \mathbf{S}_l - (\mathbf{S}_j \cdot \mathbf{S}_l)\mathbf{S}_i \times \mathbf{S}_k + (\mathbf{S}_k \cdot \mathbf{S}_l)\mathbf{S}_i \times \mathbf{S}_j). \tag{B.33}$$

There is a perfect parallel with the case of the previously-discussed isotropic 4-spin interaction. $\Omega_{iikk}^{5,4}$ does not depend on the magnetic orientations, $\Omega_{iikl}^{5,4} \propto \mathbf{S}_k \times \mathbf{S}_l$ contributes to the bilinear DMI interaction (2-spin 2-site), $\Omega_{ijij}^{5,4} \propto 2(\mathbf{S}_i \cdot \mathbf{S}_j)\mathbf{S}_i \times \mathbf{S}_j$ contributes to the CBI (4-spin 2-site), $\Omega_{ijil}^{5,4} \propto 2(\mathbf{S}_i \cdot \mathbf{S}_j)\mathbf{S}_i \times \mathbf{S}_l - \mathbf{S}_j \times \mathbf{S}_l$ gives an chiral 4-spin 3-site interaction and a correction to the bilinear DMI, and $\Omega_{ijkl}^{5,4}$ is the general form of the chiral 4-spin 4-site interaction.

The goal is to identify the simplest contributions to the electronic grand potential that potentially generate a magnetic interaction of a given type, if allowed by symmetry. Such contributions can be conveniently encoded into Feynman-like diagrams which contain the building blocks of the expansion of the grand potential, namely the Green functions of the unperturbed system and the magnetic and spin–orbit interactions at given sites. The following rules were identified from the previous case studies. A diagram that serves as a prototype for a given type of magnetic interaction is composed of:

(i) p vertices, of which $2k$ are magnetic sites (representing $\mathcal{H}^{\mathrm{mag}}$) and $p-2k$ are spin–orbit sites ($\mathcal{H}^{\mathrm{soc}}$), connected by p lines (representing $G^0(E)$).

(ii) The same magnetic site cannot appear consecutively ($G_{ii}^0(E)$ is not allowed—see analysis of $\Omega_{ijkl}^{4,4}$), but can appear repeatedly (e.g. $\Omega_{ijij}^{4,4}$).

(iii) Two spin–orbit sites cannot appear consecutively ($G^0_{ab}(E)$ is not allowed—see analysis of $\Omega^{4,2}_{ij}$), but can appear repeatedly.

(iv) The form of the magnetic interaction is obtained by taking the spin trace of the ordered product of the constituents of the diagram.

The interest is in the form of the interaction and not on the precise value of the coupling coefficient. If the latter is required the appropriate prefactor has to be determined, as shown for the discussed case studies. A diagram constructed according to these rules will give rise to a $2k$-spin interaction on n-sites ($1 \leqslant n \leqslant 2k$). If $p - 2k$ is an odd number (the spin–orbit coupling appears an odd number of times) the interaction is chiral (i.e. contains $\mathbf{S}_i \times \mathbf{S}_j$ dotted with a pseudovector, as in the DMI), otherwise it represents a symmetric anisotropic interaction (or isotropic, for $p = 2k$). The $n = 1$ diagrams contribute to the on-site magnetic anisotropy, the $n = 2$ diagrams to the pairwise magnetic interactions, and so on.

Appendix C. Symmetry rules for the prototypical diagrams

Given a pair of magnetic sites i and j connected with the vector $\mathbf{R}_{ij}$, the relevant spatial symmetries are the following: (a) inversion center in-between i and j; (b) mirror plane with $\hat{\mathbf{n}} \| \mathbf{R}_{ij}$; (c) two-fold rotation along an axis $\hat{\mathbf{n}} \perp \mathbf{R}_{ij}$, (d) mirror plane with $\hat{\mathbf{n}} \perp \mathbf{R}_{ij}$, (e) n-fold rotation along $\hat{\mathbf{n}} \| \mathbf{R}_{ij}$ with $n \geqslant 2$. All the symmetries are illustrated in figures 1(e)–(i) of the main text. The global symmetry operations can be defined as a combination of local transformations at each site (e.g. a rotation or a mirroring) and a permutation of the sites. For the pair interactions two different classes of symmetry operations can be distinguished. The first class describes global symmetry operations which permute i and j, whereas the second class describes symmetry operations which leave i and j invariant. The operations (a)–(c) fall in the first class and (d) and (e) in the second class. In terms of the diagrams a permutation of i and j corresponds to the same diagram (with labeled vertices), but with opposite direction of the Green functions. Since the local symmetry operations affect the spatial dependence of all the integration variables at the same time, those effects are not important. However, the effect of the local symmetry operation on the angular momentum operator has to be considered. The orbital angular momentum operator transforms as a pseudovector under the considered spatial symmetry operations,

$$\mathcal{I}\,\mathbf{L} = \mathbf{L}, \tag{C.1}$$

$$\mathcal{M}_{\hat{\mathbf{n}}}\mathbf{L} = \mathcal{P}^{\|}_{\hat{\mathbf{n}}}\,\mathbf{L} - \mathcal{P}^{\perp}_{\hat{\mathbf{n}}}\mathbf{L}, \tag{C.2}$$

$$\mathcal{R}_{\hat{\mathbf{n}}}(\alpha)\mathbf{L} = \mathcal{P}^{\|}_{\hat{\mathbf{n}}}\,\mathbf{L} + \cos\alpha\,\mathcal{P}^{\perp}_{\hat{\mathbf{n}}}\mathbf{L} + \sin\alpha(\hat{\mathbf{n}} \times \mathbf{L}), \tag{C.3}$$

where we used the inversion operator $\mathcal{I}$, the mirror operator $\mathcal{M}_{\hat{\mathbf{n}}}$ mirroring on the plane normal to $\hat{\mathbf{n}}$, the rotation operator $\mathcal{R}_{\hat{\mathbf{n}}}(\alpha)$ describing a rotation by α around the axis $\hat{\mathbf{n}}$, and the vector projections parallel and perpendicular to $\hat{\mathbf{n}}$, $\mathcal{P}^{\|}_{\hat{\mathbf{n}}}\,\mathbf{L} = (\hat{\mathbf{n}} \cdot \mathbf{L})\hat{\mathbf{n}}$ and $\mathcal{P}^{\perp}_{\hat{\mathbf{n}}}\mathbf{L} = \mathbf{L} - (\hat{\mathbf{n}} \cdot \mathbf{L})\hat{\mathbf{n}}$, respectively. Using these expressions it is easy to derive the so-called Moriya rules, which are the symmetry rules for the DMI vector. In total, one finds the following rules for the different symmetry operations [4, 40, 41]: (a) $\mathbf{D}_{ij} = \mathbf{0}$, (b) $\mathcal{P}^{\|}_{\hat{\mathbf{n}}}\,\mathbf{D}_{ij} = \mathbf{0}$, (c) $\mathcal{P}^{\|}_{\hat{\mathbf{n}}}\,\mathbf{D}_{ij} = \mathbf{0}$, (d) $\mathcal{P}^{\perp}_{\hat{\mathbf{n}}}\mathbf{D}_{ij} = \mathbf{0}$, and (e) $\mathcal{P}^{\perp}_{\hat{\mathbf{n}}}\mathbf{D}_{ij} = \mathbf{0}$, which is valid for the usual bilinear DMI vector $\mathbf{D}_{ij}$, as well as the CBI vector $\mathbf{C}_{ij}$.

We illustrate the derivation of the symmetry rules by analyzing the prototypical diagram that generates the DMI in the presence of a symmetry of type (b). Such a diagram connects two magnetic sites i and j to a spin–orbit site a, and this connection can be done in two ways, as illustrated in figures C1(a), (b). The mirror plane ensures the existence of another spin–orbit site $b = \mathcal{M}_{\hat{\mathbf{n}}}\,a$, located at the mirror position of a. This generates another pair of diagrams, as shown in figures C1(c), (d). Omitting the energy dependence, the corresponding integration and other details, we can represent the structure of these diagrams as follows:

$$(1a) \rightarrow \ \mathrm{Tr}\ G^0_{ai}\,U_i\,G^0_{ij}\,U_j\,G^0_{ja}\,\lambda_a\,\mathbf{L}\cdot(\mathbf{S}_i \times \mathbf{S}_j), \tag{C.4}$$

$$(1b) \rightarrow \ \mathrm{Tr}\ G^0_{aj}\,U_j\,G^0_{ji}\,U_i\,G^0_{ia}\,\lambda_a\,\mathbf{L}\cdot(\mathbf{S}_j \times \mathbf{S}_i), \tag{C.5}$$

$$(1c) \rightarrow \ \mathrm{Tr}\ G^0_{bj}\,U_j\,G^0_{ji}\,U_i\,G^0_{ib}\,\lambda_b\,\mathbf{L}\cdot(\mathbf{S}_j \times \mathbf{S}_i), \tag{C.6}$$

$$(1d) \rightarrow \ \mathrm{Tr}\ G^0_{bi}\,U_i\,G^0_{ij}\,U_j\,G^0_{jb}\,\lambda_b\,\mathbf{L}\cdot(\mathbf{S}_i \times \mathbf{S}_j). \tag{C.7}$$

The orientations of the magnetic moments, and so also $\mathbf{S}_i \times \mathbf{S}_j$, are kept fixed for all diagrams. From the geometry alone, and with $M_{\hat{\mathbf{n}}}$ representing the spatial mirror operator in our chosen Wannier-like basis, we have $M_{\hat{\mathbf{n}}}\,G^0_{ij}M^{-1}_{\hat{\mathbf{n}}} = G^0_{ji}$, $M_{\hat{\mathbf{n}}}\,G^0_{ja}M^{-1}_{\hat{\mathbf{n}}} = G^0_{ib}$, and $M_{\hat{\mathbf{n}}}\,G^0_{ai}M^{-1}_{\hat{\mathbf{n}}} = G^0_{bj}$, among other relations. We can then rewrite

$$(1c) \rightarrow \ \mathrm{Tr}\ M_{\hat{\mathbf{n}}}\,G^0_{ai}M^{-1}_{\hat{\mathbf{n}}}U_j\,M_{\hat{\mathbf{n}}}\,G^0_{ij}M^{-1}_{\hat{\mathbf{n}}}U_i\,M_{\hat{\mathbf{n}}}\,G^0_{ja}M^{-1}_{\hat{\mathbf{n}}}\lambda_b\,\mathbf{L}\cdot(\mathbf{S}_j \times \mathbf{S}_i) \tag{C.8}$$

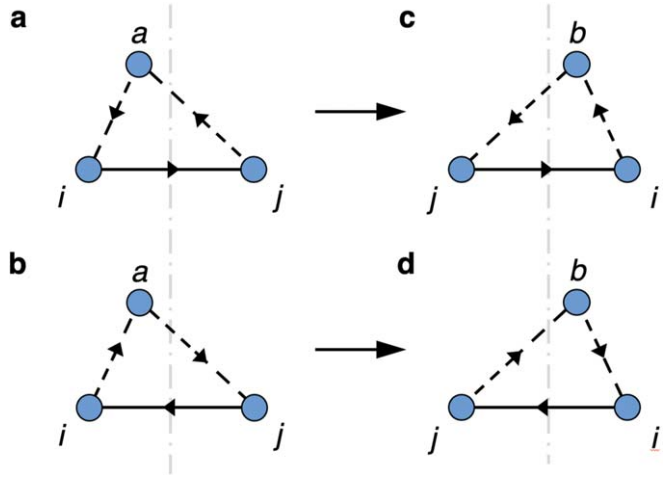

Figure C1. Symmetry-related prototypical diagrams. As an example, we select the diagram generating the DMI in a system where a mirror plane perpendicular to the bond is present. This ensures that there is a spin–orbit site $b = \mathcal{M}a$, that is, located at the mirrored position of a. The two magnetic sites i and j and the spin–orbit site a can be connected in the ways shown in (a) and (b). Likewise, the two magnetic sites i and j and the spin–orbit site b can be connected in the ways shown in (c) and (d). We show that (a) can be related to (c) and that (b) can be related to (d).

$$= \mathrm{Tr}\, G^0_{ai}\, U_i\, G^0_{ij}\, U_j\, G^0_{ja}\, \lambda_a (M^{-1}_{\hat{\mathbf{n}}} \mathbf{L}\, M_{\hat{\mathbf{n}}}) \cdot (\mathbf{S}_j \times \mathbf{S}_i) \tag{C.9}$$

$$= \mathrm{Tr}\, G^0_{ai}\, U_i\, G^0_{ij}\, U_j\, G^0_{ja}\, \lambda_a (P^{\perp}_{\hat{\mathbf{n}}} \mathbf{L} - P^{\parallel}_{\hat{\mathbf{n}}} \mathbf{L}) \cdot (\mathbf{S}_i \times \mathbf{S}_j), \tag{C.10}$$

where we used that $U_i = M^{-1}_{\hat{\mathbf{n}}} U_j M_{\hat{\mathbf{n}}}$, $\lambda_a = M^{-1}_{\hat{\mathbf{n}}} \lambda_b M_{\hat{\mathbf{n}}}$ and equation (C.2). Combining this result with the one for (1a) and using $\mathbf{L} = \mathcal{P}^{\perp}_{\hat{\mathbf{n}}} \mathbf{L} + \mathcal{P}^{\parallel}_{\hat{\mathbf{n}}} \mathbf{L}$, we arrive at the final expression

$$\begin{aligned} (1a) + (1c) &\to 2\, \mathrm{Tr}\, G^0_{ai}\, U_i\, G^0_{ij}\, U_j\, G^0_{ja}\, \lambda_a (\mathcal{P}^{\perp}_{\hat{\mathbf{n}}} \mathbf{L}) \cdot (\mathbf{S}_i \times \mathbf{S}_j) \\ &\sim \mathcal{P}^{\perp}_{\hat{\mathbf{n}}} \mathbf{D}_{ij} \cdot (\mathbf{S}_i \times \mathbf{S}_j). \end{aligned} \tag{C.11}$$

This corresponds precisely to Moriya's rule (b) $\mathcal{P}^{\parallel}_{\hat{\mathbf{n}}}\, \mathbf{D}_{ij} = \mathbf{0}$, and a similar conclusion can be reached by combining diagrams (1b) and (1d). Following similar steps for each kind of symmetry (i.e. identifying all symmetry-related spin–orbit sites, and combining the related prototypical diagrams using the transformation properties of $\mathbf{L}$) it is straightforward to derive all of Moriya's rules and to show that no further effort is required to conclude that they also apply to the CBI vector.

Appendix D. Relation between the spin cluster expansion and the generalized Heisenberg model

To analyze our DFT data, we make use of the spin cluster expansion [52, 53]. Each spin magnetic moment is represented by a classical unit vector $\mathbf{S}_i = (\cos\varphi_i \sin\vartheta_i,\ \sin\varphi_i \sin\vartheta_i,\ \cos\vartheta_i)$. The energy of a magnetic system with pair interactions can then be parametrized using a systematic expansion in terms of real spherical harmonics $Y_{L_i}(\vartheta_i,\ \varphi_i)$ as

$$E_{\mathrm{SCE}}[\{\mathbf{S}\}] = \sum_i \sum_{L_i \neq 0} K_i^{L_i} Y_{L_i}(\vartheta_i,\ \varphi_i) + \frac{1}{2} \sum_{\substack{i,j \\ i \neq j}} \sum_{\substack{L_i \neq 0 \\ L_j \neq 0}} J_{ij}^{L_i L_j} Y_{L_i}(\vartheta_i,\ \varphi_i)\, Y_{L_j}(\vartheta_j,\ \varphi_j), \tag{D.1}$$

where $L_i = (\ell_i, m_i)$ is a combined spherical harmonic index. Since the total energy has to be even under time-reversal (which inverts the orientation of the magnetic moments), only coefficients with even total $\ell = \sum_i \ell_i$ are allowed. This means that ℓ_i has to be even for the on-site anisotropy coefficients $K_i^{L_i}$, and that the sum $\ell_i + \ell_j$ has to be even for the pair interaction coefficients $J_{ij}^{L_i L_j}$. The bilinear magnetic interaction is given by the $\ell_i = \ell_j = 1$ elements of $J_{ij}^{L_i L_j}$, whereas the biquadratic magnetic interaction is given by the $\ell_i = \ell_j = 2$ ones. In agreement with our discussion in the main text, the biquadratic interaction is thus determined by at most $5 \times 5 = 25$ independent variables.

In the main text, we discuss the different magnetic interactions using the more conventional representation in terms of cartesian unit vector components,

$$E_{\mathrm{DFT}}[\{\mathbf{S}\}] = \sum_i \sum_{\alpha,\beta} K_i^{\alpha\beta} S_i^\alpha S_i^\beta + \frac{1}{2}\sum_{i,j}\sum_{\alpha,\beta} J_{ij}^{\alpha\beta} S_i^\alpha S_j^\beta + \frac{1}{2}\sum_{i,j}\sum_{\alpha,\beta,\gamma,\delta} B_{ij}^{\alpha\beta\gamma\delta} S_i^\alpha S_j^\beta S_i^\gamma S_j^\delta. \tag{D.2}$$

This representation has a simple relation to the spherical harmonic expansion used in the spin cluster expansion. We first express the components of the unit vectors in terms of spherical harmonics, $S^\alpha = x^\alpha/r = \sqrt{4\pi/3}\ Y_{L^\alpha}(\vartheta,\ \varphi)$ with $L^x = (1,1), L^y = (1,\ -\ 1)$ and $L^z = (1,0)$. We then use Gaunt coefficients to rewrite the product of two spherical harmonics for the same direction in terms of a single one,

$$S^\alpha S^\beta = \frac{4\pi}{3}\sum_L C^L_{L^\alpha L^\beta} Y_L(\vartheta,\ \varphi). \tag{D.3}$$

The Gaunt coefficients obey the basic properties: $\ell^\alpha + \ell^\beta + \ell$ must be even, $|\ell^\alpha - \ell^\beta| \leqslant \ell \leqslant \ell^\alpha + \ell^\beta$ (triangle inequality), and $C^L_{L^\alpha L^\beta} = C^L_{L^\beta L^\alpha}$. In this way we find a connection between the two representations. The onsite anisotropy coefficients are related by

$$K_i^{L_i} = \frac{4\pi}{3}\sum_{\alpha,\beta} C^{L_i}_{L_i^\alpha L_i^\beta} K_i^{\alpha\beta}, \tag{D.4}$$

the bilinear interaction coefficients by

$$J_{ij}^{L_i^\alpha L_j^\beta} = \frac{4\pi}{3} J_{ij}^{\alpha\beta}, \tag{D.5}$$

and the biquadratic interaction coefficients by

$$B_{ij}^{L_i L_j} = \left(\frac{4\pi}{3}\right)^2 \sum_{\alpha\beta\gamma\delta} B_{ij}^{\alpha\beta\gamma\delta} C^{L_i}_{L^\alpha L^\gamma} C^{L_j}_{L^\beta L^\delta}. \tag{D.6}$$

Appendix E. Micromagnetic form of the CBI

To arrive at the micromagnetic form of the interactions discussed in this work, consider the following coarse-graining procedure. We first consider all the magnetic sites connected to a reference site i, to define its contribution to the magnetic energy. We can then find the value of the micromagnetic energy at the point $\mathbf{R}_i$ by calculating the magnetic energy in the spin model:

$$\mathcal{E}(\mathbf{R}_i) = \sum_j (J_{ij}\,\mathbf{S}_i\cdot\mathbf{S}_j + \mathbf{D}_{ij}\cdot(\mathbf{S}_i\times\mathbf{S}_j) + B_{ij}(\mathbf{S}_i\cdot\mathbf{S}_j)^2 + \mathbf{C}_{ij}\cdot(\mathbf{S}_i\times\mathbf{S}_j)(\mathbf{S}_i\cdot\mathbf{S}_j)). \tag{E.1}$$

The orientation of the lattice spins is obtained from a smoothly varying spin field which is approximated by its average direction and its gradient at the point $\mathbf{R}_i$, with $\mathbf{R}_{ij} = \mathbf{R}_j - \mathbf{R}_i$,

$$\mathbf{S}_j \approx \mathbf{S}_i + \sum_\alpha R_{ij,\alpha}\partial_\alpha \mathbf{S}_i + \frac{1}{2}\sum_{\alpha,\beta} R_{ij,\alpha}R_{ij,\beta}\,\partial_\alpha\partial_\beta \mathbf{S}_i. \tag{E.2}$$

Then

$$\mathbf{S}_i\cdot\mathbf{S}_j \approx \mathbf{S}_i\cdot\mathbf{S}_i + \sum_\alpha R_{ij,\alpha}\,\mathbf{S}_i\cdot\partial_\alpha\mathbf{S}_i + \frac{1}{2}\sum_{\alpha,\beta} R_{ij,\alpha}R_{ij,\beta}\,\mathbf{S}_i\cdot\partial_\alpha\partial_\beta\mathbf{S}_i \tag{E.3}$$

$$= 1 - \frac{1}{2}\sum_{\alpha,\beta} R_{ij,\alpha}R_{ij,\beta}(\partial_\alpha\mathbf{S}_i)\cdot(\partial_\beta\mathbf{S}_i), \tag{E.4}$$

where the last line applies if the spin field is a unit vector field: $\mathbf{S}_i\cdot\mathbf{S}_i = 1 \Rightarrow \mathbf{S}_i\cdot(\partial_\alpha\partial_\beta\mathbf{S}_i) = -(\partial_\alpha\mathbf{S}_i)\cdot(\partial_\beta\mathbf{S}_i)$. Similarly,

$$\mathbf{S}_i\times\mathbf{S}_j = \sum_\alpha R_{ij,\alpha}\,\mathbf{S}_i\times\partial_\alpha\mathbf{S}_i. \tag{E.5}$$

We then find:

(i) The exchange stiffness,

$$\begin{aligned}\sum_j J_{ij}\,\mathbf{S}_i\cdot\mathbf{S}_j &= \sum_j J_{ij}+\sum_{\alpha,\beta}\left[-\frac{1}{2}\sum_j R_{ij,\alpha}R_{ij,\beta}\,J_{ij}\right](\partial_\alpha\mathbf{S}_i)\cdot(\partial_\beta\mathbf{S}_i)\\ &= J_i+\sum_{\alpha,\beta}A^J_{i,\alpha\beta}(\partial_\alpha\mathbf{S}_i)\cdot(\partial_\beta\mathbf{S}_i),\end{aligned}\tag{E.6}$$

where the stiffness tensor is symmetric, $\mathcal{A}^J_{i,\alpha\beta}=\mathcal{A}^J_{i,\beta\alpha}$, and expresses the spatial anisotropy of the material.

(ii) The micromagnetic DMI,

$$\begin{aligned}\sum_j \mathbf{D}_{ij}\cdot(\mathbf{S}_i\times\mathbf{S}_j) &= \sum_\alpha\left[\sum_j R_{ij,\alpha}\,\mathbf{D}_{ij}\right]\cdot(\mathbf{S}_i\times(\partial_\alpha\mathbf{S}_i))\\ &= \sum_\alpha \boldsymbol{\mathcal{D}}^D_{i,\alpha}\cdot(\mathbf{S}_i\times(\partial_\alpha\mathbf{S}_i)).\end{aligned}\tag{E.7}$$

Here $\boldsymbol{\mathcal{D}}^D_{i,\alpha}$ is the spiralization tensor, which is contracted with the usual Lifshitz invariants $L^\alpha_{\mu\nu}=S_\mu(\partial_\alpha S_\nu)-S_\nu(\partial_\alpha S_\mu)$.

(iii) The contribution of the isotropic biquadratic interaction to the exchange stiffness, plus a new term with four derivatives,

$$\begin{aligned}\sum_j B_{ij}(\mathbf{S}_i\cdot\mathbf{S}_j)^2 &= \sum_j B_{ij}+\sum_{\alpha,\beta}\left[-\sum_j R_{ij,\alpha}R_{ij,\beta}\,B_{ij}\right](\partial_\alpha\mathbf{S}_i)\cdot(\partial_\beta\mathbf{S}_i)\\ &\quad+\sum_{\alpha,\beta,\gamma,\delta}(\partial_\alpha\mathbf{S}_i)\cdot(\partial_\beta\mathbf{S}_i)\left[\frac{1}{4}\sum_j R_{ij,\alpha}R_{ij,\beta}\,R_{ij,\gamma}R_{ij,\delta}\,B_{ij}\right](\partial_\gamma\mathbf{S}_i)\cdot(\partial_\delta\mathbf{S}_i)\\ &= \mathcal{B}_i+\sum_{\alpha,\beta}\mathcal{A}^B_{i,\alpha\beta}(\partial_\alpha\mathbf{S}_i)\cdot(\partial_\beta\mathbf{S}_i)\\ &\quad+\sum_{\alpha,\beta,\gamma,\delta}(\partial_\alpha\mathbf{S}_i)\cdot(\partial_\beta\mathbf{S}_i)\mathcal{B}_{i,\alpha\beta\gamma\delta}(\partial_\gamma\mathbf{S}_i)\cdot(\partial_\delta\mathbf{S}_i).\end{aligned}\tag{E.8}$$

(iv) The contribution of the CBI to the total micromagnetic DMI, plus a new term with three derivatives,

$$\begin{aligned}\sum_j \mathbf{C}_{ij}\cdot(\mathbf{S}_i\times\mathbf{S}_j)(\mathbf{S}_i\cdot\mathbf{S}_j) &= \sum_\alpha\left[\sum_j R_{ij,\alpha}\,\mathbf{C}_{ij}\right]\cdot(\mathbf{S}_i\times(\partial_\alpha\mathbf{S}_i))\\ &\quad+\sum_{\alpha,\beta,\gamma}\left[-\frac{1}{2}\sum_j R_{ij,\alpha}R_{ij,\beta}R_{ij,\gamma}\,\mathbf{C}_{ij}\right]\cdot(\mathbf{S}_i\times(\partial_\alpha\mathbf{S}_i))(\partial_\beta\mathbf{S}_i)\cdot(\partial_\gamma\mathbf{S}_i)\\ &= \sum_\alpha \boldsymbol{\mathcal{D}}^C_{i,\alpha}\cdot(\mathbf{S}_i\times\partial_\alpha\mathbf{S}_i)\\ &\quad+\sum_{\alpha,\beta,\gamma}\boldsymbol{\mathcal{C}}_{i,\alpha\beta\gamma}\cdot(\mathbf{S}_i\times\partial_\alpha\mathbf{S}_i)(\partial_\beta\mathbf{S}_i)\cdot(\partial_\gamma\mathbf{S}_i).\end{aligned}\tag{E.9}$$

All the interaction tensors are invariant under arbitrary permutations of the indices $\alpha,\beta,\gamma,\delta$. Assuming that the material is sufficiently isotropic, so that the micromagnetic parameters become independent of position, the complete micromagnetic energy for an arbitrary point in the magnetic material can then be expressed as (omitting the previously found constants and collecting all terms of the same form)

$$\begin{aligned}\mathcal{E}(\mathbf{r}) &= \sum_{\alpha,\beta}\mathcal{A}_{\alpha\beta}(\partial_\alpha\mathbf{S}(\mathbf{r}))\cdot(\partial_\beta\mathbf{S}(\mathbf{r}))+\sum_\alpha\boldsymbol{\mathcal{D}}_\alpha\cdot(\mathbf{S}(\mathbf{r})\times\partial_\alpha\mathbf{S}(\mathbf{r}))\\ &\quad+\sum_{\alpha,\beta,\gamma,\delta}(\partial_\alpha\mathbf{S}(\mathbf{r}))\cdot(\partial_\beta\mathbf{S}(\mathbf{r}))\mathcal{B}_{\alpha\beta\gamma\delta}(\partial_\gamma\mathbf{S}(\mathbf{r}))\cdot(\partial_\delta\mathbf{S}(\mathbf{r}))\\ &\quad+\sum_{\alpha,\beta,\gamma}\boldsymbol{\mathcal{C}}_{\alpha\beta\gamma}\cdot(\mathbf{S}(\mathbf{r})\times\partial_\alpha\mathbf{S}(\mathbf{r}))(\partial_\beta\mathbf{S}(\mathbf{r}))\cdot(\partial_\gamma\mathbf{S}(\mathbf{r})).\end{aligned}\tag{E.10}$$

The total micromagnetic energy is then given by forming the corresponding energy density (dividing by the volume per magnetic site, $V_0 = V/N$) and integrating over the volume of the material,

$$E_{\text{micro}} = \int \mathrm{d}V\ \widetilde{\mathcal{E}}(\mathbf{r}), \qquad \widetilde{\mathcal{E}}(\mathbf{r}) = \frac{\mathcal{E}(\mathbf{r})}{V_0}. \tag{E.11}$$

The micromagnetic parameters must also be divided by V_0, for consistency. For a simple cubic lattice with the lattice constant a and nearest-neighbor interactions ($J_{ij} = -\,\mathrm{J}$ and $B_{ij} = B$, and the vectors $\mathbf{D}_{ij}$ and $\mathbf{C}_{ij}$ along the nearest-neighbor directions and with magnitude D and C, respectively), the general forms of the micromagnetic interaction densities simplify further.

(i) For the exchange stiffness one finds,

$$\widetilde{\mathcal{E}}^{\mathrm{A}}(\mathbf{r}) = \frac{J - 2B}{a}\left[\left(\frac{\partial \mathbf{S}}{\partial x}\right)^2 + \left(\frac{\partial \mathbf{S}}{\partial y}\right)^2 + \left(\frac{\partial \mathbf{S}}{\partial z}\right)^2\right]. \tag{E.12}$$

(ii) For the micromagnetic DMI one finds,

$$\widetilde{\mathcal{E}}^{\mathrm{DMI}}(\mathbf{r}) = \frac{2(D + C)}{a^2}\ \mathbf{S}(\mathbf{r}) \cdot (\boldsymbol{\nabla} \times \mathbf{S}(\mathbf{r})). \tag{E.13}$$

(iii) For the micromagnetic isotropic biquadratic interaction one finds,

$$\widetilde{\mathcal{E}}^{\mathrm{B}}(\mathbf{r}) = \frac{Ba}{2}\left[\left(\frac{\partial \mathbf{S}}{\partial x}\right)^4 + \left(\frac{\partial \mathbf{S}}{\partial y}\right)^4 + \left(\frac{\partial \mathbf{S}}{\partial z}\right)^4\right]. \tag{E.14}$$

(iv) Last, for the micromagnetic CBI one finds using the Lifshitz invariants,

$$\begin{aligned}\widetilde{\mathcal{E}}^{\mathrm{CBI}}(\mathbf{r}) &= -C\sum_{\alpha}(\mathbf{S}_i \times \partial_\alpha \mathbf{S}_i)_\alpha (\partial_\alpha \mathbf{S}_i) \cdot (\partial_\alpha \mathbf{S}_i) \\ &= -C\left[L^x_{yz}\left(\frac{\partial \mathbf{S}}{\partial x}\right)^2 + L^y_{zx}\left(\frac{\partial \mathbf{S}}{\partial y}\right)^2 + L^z_{xy}\left(\frac{\partial \mathbf{S}}{\partial z}\right)^2\right].\end{aligned} \tag{E.15}$$

Appendix F. Parametrization of the magnetic hamiltonian for dimers on Pt(111), Ir(111), Pt(001) and Re(0001)

The torques for the different non-collinear configurations were used to fully parametrize the dimers on the different surfaces. For the (111) facet of Pt and Ir, and the Re(0001) surface, the dimers are placed along the x-axis with a mirror plane spanned by yz-plane as depicted in figure 2. The on-site anisotropy matrix of the first atom is related to that of the second atom by $K_2 = \mathcal{M}_x K_1 \mathcal{M}_x$, where $\mathcal{M}_x$ is the mirror operator for a mirror plane perpendicular to the x-axis. Since the trace of the on-site anisotropy matrix yields a constant energy shift, we set $K^{zz} = 0$. For the bilinear exchange matrix one finds $J_{12} = \mathcal{M}_x J_{21} \mathcal{M}_x = \mathcal{M}_x J_{12}^{\mathrm{T}} \mathcal{M}_x$, which restricts the DM vector to $\mathbf{D}_{12} = (0,\ D^y_{12},\ D^z_{12})$ and the only off-diagonal component of the symmetric exchange is J^{yz}_{12}. For the biquadratic exchange one finds $B_{12}^{\alpha\beta\gamma\delta} = (-1)^{N_x} B_{12}^{\beta\alpha\delta\gamma}$, where N_x is the number of times x appears in $\alpha\,\beta\,\gamma\,\delta$. In case of the Pt(001) surface, there is one additional mirror plane resulting in further constraints due to $\mathcal{M}_y$, the mirror operator for a mirror plane perpendicular to the y-axis. The on-site anisotropies fulfill a local symmetry $K_1 = \mathcal{M}_y K_1 \mathcal{M}_y$ yielding $K^{xy} = K^{yz} = 0$. The pair interactions fulfill the same symmetry $J_{12} = \mathcal{M}_y J_{12} \mathcal{M}_y$ yielding D^y as the only finite off-diagonal component. For the biquadratic tensor the additional constrain follows from $B_{12}^{\alpha\beta\gamma\delta} = (-1)^{N_y} B_{12}^{\alpha\beta\gamma\delta}$, where N_y is the number of times y appears in $\alpha\,\beta\,\gamma\,\delta$. The irreducible components for the different surfaces are shown in tables F1–F4.

Table F1. Independent exchange parameters of the Cr, Mn, Fe, Co and Ni dimers on the Pt(111) surface in (meV) and the canting angles using the full parametrization, $\Delta\alpha^{\text{full}}$, or different combinations of the isotropic bilinear interaction J, the isotropic biquadratic interaction B and the y-components of the DMI D and CBI C.

Pt(111)	Cr	Mn	Fe	Co	Ni
K_1^{xx}	−1.23	−0.49	0.14	3.14	0.60
K_1^{xy}	−0.24	0.13	0.23	0.34	0.02
K_1^{xz}	−0.18	0.15	0.42	0.17	−0.01
K_1^{yy}	−2.24	0.02	1.27	3.66	0.64
K_1^{yz}	0.08	−0.23	−0.06	0.01	−0.04
J_{12}^{xx}	36.30	59.02	−43.65	−76.89	−5.36
J_{12}^{yy}	34.94	58.63	−41.80	−76.96	−5.28
J_{12}^{zz}	36.23	57.94	−43.45	−76.52	−5.59
J_{12}^{yz}	0.26	0.42	−0.33	−1.11	−0.11
D_{12}^{y}	8.54	−3.30	−7.27	7.06	0.75
D_{12}^{z}	1.85	−0.13	0.30	−3.57	−0.37
B_{12}^{xxxx}	−8.99	0.56	−1.57	0.61	−0.87
B_{12}^{xxxy}	−0.08	−0.02	−0.05	−0.09	−0.08
B_{12}^{xxxz}	−1.28	0.31	−1.28	0.82	−0.22
B_{12}^{xxyy}	−6.83	0.43	−1.40	0.67	−0.67
B_{12}^{xxyz}	−0.00	0.00	−0.01	0.08	−0.01
B_{12}^{xxzz}	−6.72	0.42	−1.06	0.26	−0.65
B_{12}^{xyxy}	4.47	−0.31	1.01	−0.53	0.44
B_{12}^{xyxz}	0.03	−0.01	−0.03	−0.06	0.01
B_{12}^{xyyy}	−0.04	−0.03	−0.02	−0.14	−0.08
B_{12}^{xyyz}	−0.59	0.15	−0.67	0.39	−0.11
B_{12}^{xyzy}	−0.01	0.00	0.00	−0.01	0.00
B_{12}^{xyzz}	0.00	−0.02	−0.02	−0.02	−0.04
B_{12}^{yyyy}	−8.90	0.66	−1.95	0.74	−0.90
B_{12}^{yyyz}	−0.02	−0.00	0.04	0.03	−0.01
B_{12}^{yyzz}	−6.66	0.56	−1.24	0.35	−0.64
$\Delta\alpha^{\text{full}}$	−3°	3°	7°	−4°	−8°
$\Delta\alpha^{\text{J+D}}$	−13°	3°	10°	−5°	−8°
$\Delta\alpha^{\text{J+D+C}}$	−10°	3°	6°	−4°	−13°
$\Delta\alpha^{\text{J+D+C+B}}$	−6°	3°	6°	−4°	−10°

Additionally, the canting angles obtained from minimizing a Heisenberg model containing the full parametrizations, $\Delta\alpha^{\text{full}}$, and the canting angles obtained from a simplified model containing different combinations of pair interactions (see equation (9)) are shown in the tables F1–F4. The canting angles $\Delta\alpha^{\text{full}}$ should be closest to the realistic values, since they include the effect of the magnetic anisotropy, which in particular becomes relevant if $\max(|K^{\alpha\beta}|) \gtrsim |\mathbf{D}|, |\mathbf{C}|$. For example for the Co dimer on Re(0001) the anisotropy dominates the canting angles resulting in $\Delta\alpha^{\text{full}} = -63°$ for the full parametrization, while all the pair interactions result in $\Delta\alpha^{\text{J+D+C+B}} = 20°$. For most of the other considered dimer the effect of the anisotropy is small.

Table F2. Independent exchange parameters of the Cr, Mn, Fe and Co dimers on the Pt(001) surface in (meV) and the canting angles using the full parametrization, $\Delta\alpha^{\text{full}}$, or different combinations of the isotropic bilinear interaction J, the isotropic biquadratic interaction B and the y-components of the DMI D and CBI C.

Pt(001)	Cr	Mn	Fe	Co
K_1^{xx}	−0.40	−1.48	0.45	−0.03
K_1^{xz}	−0.21	0.40	−0.18	−0.08
K_1^{yy}	−0.84	−2.08	0.50	0.75
J_{12}^{xx}	−34.56	52.92	13.78	−46.67
J_{12}^{yy}	−35.67	52.31	15.61	−48.48
J_{12}^{zz}	−35.60	50.52	15.61	−43.77
D_{12}^{y}	11.22	−2.52	−9.57	4.50
B_{12}^{xxxx}	−7.47	1.27	−1.13	−1.55
B_{12}^{xxxz}	−1.22	0.05	0.12	−0.21
B_{12}^{xxyy}	−5.62	0.90	−0.82	−1.20
B_{12}^{xxzz}	−5.61	1.02	−0.84	−1.10
B_{12}^{xyxy}	3.76	−0.62	0.49	0.84
B_{12}^{xyyz}	−0.62	0.02	0.06	−0.13
B_{12}^{yyyy}	−7.44	1.26	−1.06	−1.57
B_{12}^{yyzz}	−5.44	0.96	−0.90	−1.10
$\Delta\alpha^{\text{full}}$	−14°	0°	28°	0°
$\Delta\alpha^{\text{J+D}}$	−18°	3°	32°	−6°
$\Delta\alpha^{\text{J+D+C}}$	−21°	3°	32°	−6°
$\Delta\alpha^{\text{J+D+C+B}}$	−14°	3°	28°	−6°

Table F3. Independent exchange parameters of the Cr, Mn, Fe and Co dimers on the Ir(111) surface in (meV) and the canting angles using the full parametrization, $\Delta\alpha^{\text{full}}$, or different combinations of the isotropic bilinear interaction J, the isotropic biquadratic interaction B and the y-components of the DMI D and CBI C.

Ir(111)	Cr	Mn	Fe	Co
K_1^{xx}	−0.12	−3.07	−2.44	0.07
K_1^{xy}	−0.24	−0.22	0.47	0.26
K_1^{xz}	−0.08	−0.14	−0.13	−0.11
K_1^{yy}	−0.66	−3.26	−0.92	1.13
K_1^{yz}	0.40	0.46	−0.37	−0.21
J_{12}^{xx}	29.81	55.57	−16.33	−60.76
J_{12}^{yy}	28.51	55.32	−15.38	−60.69
J_{12}^{zz}	30.08	54.80	−17.15	−60.21
J_{12}^{yz}	−0.09	0.22	−0.03	−0.13
D_{12}^{y}	−10.71	1.74	14.65	3.00
D_{12}^{z}	−0.48	0.07	−0.17	−1.77
B_{12}^{xxxx}	−9.29	1.08	−2.94	0.71
B_{12}^{xxxy}	0.29	−0.03	0.03	0.08
B_{12}^{xxxz}	1.62	0.19	0.71	0.01
B_{12}^{xxyy}	−7.02	0.55	−2.14	0.56
B_{12}^{xxyz}	0.01	−0.12	−0.01	0.00
B_{12}^{xxzz}	−6.89	0.91	−2.21	0.51
B_{12}^{xyxy}	4.75	−0.46	1.41	−0.38
B_{12}^{xyxz}	−0.01	0.21	−0.02	0.00
B_{12}^{xyyy}	0.31	0.03	0.04	0.06
B_{12}^{xyyz}	0.78	0.05	0.32	0.03
B_{12}^{xyzy}	−0.01	−0.05	0.01	−0.03
B_{12}^{xyzz}	0.17	0.04	0.03	0.04
B_{12}^{yyyy}	−9.43	0.73	−2.71	0.61
B_{12}^{yyyz}	0.01	−0.14	0.01	0.00
B_{12}^{yyzz}	−6.97	0.83	−2.01	0.43
$\Delta\alpha^{\text{full}}$	−6°	0°	27°	4°
$\Delta\alpha^{\text{J+D}}$	−20°	2°	42°	3°
$\Delta\alpha^{\text{J+D+C}}$	−15°	2°	41°	3°
$\Delta\alpha^{\text{J+D+C+B}}$	−8°	2°	32°	3°

Table F4. Independent exchange parameters of the Cr, Mn, Fe and Co dimers on the Re(0001) surface in (meV) and the canting angles using the full parametrization, $\Delta\alpha^{\text{full}}$, or different combinations of the isotropic bilinear interaction J, the isotropic biquadratic interaction B and the y-components of the DMI D and CBI C.

Re(0001)	Cr	Mn	Fe	Co
K_1^{xx}	2.48	1.31	−0.39	−2.44
K_1^{xy}	0.42	0.05	0.08	−0.90
K_1^{xz}	−0.15	0.29	-0.07	−2.17
K_1^{yy}	2.18	0.90	−0.93	0.56
K_1^{yz}	−1.44	−0.65	−0.08	−1.06
J_{12}^{xx}	−16.31	−16.05	−2.35	−0.05
J_{12}^{yy}	−17.56	−18.67	−2.43	−4.47
J_{12}^{zz}	−15.40	−15.81	−2.02	−3.71
J_{12}^{yz}	−0.44	−1.10	0.01	0.32
D_{12}^{y}	18.06	15.55	−0.50	−1.05
D_{12}^{z}	2.97	3.09	−0.78	−1.20
B_{12}^{xxxx}	−2.67	−2.24	0.06	0.00
B_{12}^{xxxy}	−0.02	0.10	−0.14	−1.26
B_{12}^{xxxz}	0.10	−0.43	0.16	−0.80
B_{12}^{xxyy}	−2.03	−1.62	0.04	−0.09
B_{12}^{xxyz}	−0.11	−0.00	0.01	−0.02
B_{12}^{xxzz}	−1.88	−1.63	0.07	−0.12
B_{12}^{xyxy}	1.42	1.10	−0.01	−0.00
B_{12}^{xyxz}	0.04	−0.05	−0.03	0.34
B_{12}^{xyyy}	0.01	0.08	−0.14	−0.31
B_{12}^{xyyz}	0.13	−0.18	0.09	0.43
B_{12}^{xyzy}	−0.09	0.00	−0.01	−0.13
B_{12}^{xyzz}	0.02	0.05	−0.05	0.00
B_{12}^{yyyy}	−2.67	−2.10	0.07	0.00
B_{12}^{yyyz}	−0.00	0.01	0.01	−0.18
B_{12}^{yyzz}	−1.88	−1.60	0.04	0.21
$\Delta\alpha^{\text{full}}$	33°	30°	−17°	−63°
$\Delta\alpha^{J+D}$	48°	41°	−12°	20°
$\Delta\alpha^{J+D+C}$	48°	41°	−18°	22°
$\Delta\alpha^{J+D+C+B}$	40°	35°	−19°	22°

ORCID iDs

Sascha Brinker https://orcid.org/0000-0002-7077-1244
Manuel dos Santos Dias https://orcid.org/0000-0002-8835-5580
Samir Lounis https://orcid.org/0000-0003-2573-2841

References

[1] Heisenberg W 1928 *Z. Phys.* **49** 619–36
[2] van Vleck J H 1937 *Phys. Rev.* **52** 1178–98
[3] Dzyaloshinsky I 1958 *J. Phys. Chem. Solids* **4** 241–55
[4] Moriya T 1960 *Phys. Rev.* **120** 91–8
[5] Anderson P W 1963 Theory of magnetic exchange interactions: exchange in insulators and semiconductors *Solid State Physics* vol 14 ed F Seitz and D Turnbull (New York: Academic) pp 99–214
[6] Fawcett E 1988 *Rev. Mod. Phys.* **60** 209
[7] Rührig M, Schäfer R, Hubert A, Mosler R, Wolf J, Demokritov S and Grünberg P 1991 *Phys. Status Solidi* a **125** 635–56
[8] Katsura H, Nagaosa N and Balatsky A V 2005 *Phys. Rev. Lett.* **95** 057205
[9] Mostovoy M 2006 *Phys. Rev. Lett.* **96** 067601
[10] Lounis S, Dederichs P H and Blügel S 2008 *Phys. Rev. Lett.* **101** 107204
[11] Jackeli G and Khaliullin G 2009 *Phys. Rev. Lett.* **102** 017205
[12] Roger M, Hetherington J H and Delrieu J M 1983 *Rev. Mod. Phys.* **55** 1–64
[13] Takahashi M 1977 *J. Phys. C: Solid State Phys.* **10** 1289–7301
[14] MacDonald A H, Girvin S M and Yoshioka D 1988 *Phys. Rev.* B **37** 9753–6
[15] Michaud F, Vernay F, Manmana S R and Mila F 2012 *Phys. Rev. Lett.* **108** 127202
[16] Hoffmann M and Blügel S 2018 arXiv:1803.01315

[17] Batista C D, Lin S Z, Hayami S and Kamiya Y 2016 *Rep. Prog. Phys.* **79** 084504
[18] Ozawa R, Hayami S and Motome Y 2017 *Phys. Rev. Lett.* **118** 147205
[19] Hayami S, Ozawa R and Motome Y 2017 *Phys. Rev.* B **95** 224424
[20] Al-Zubi A, Bihlmayer G and Blügel S 2011 *Phys. Status Solidi* b **248** 2242–7
[21] Krönlein A *et al* 2018 *Phys. Rev. Lett.* **120** 207202
[22] Kurz P, Bihlmayer G, Hirai K and Blügel S 2001 *Phys. Rev. Lett.* **86** 1106–9
[23] Bogdanov A and Yablonskii D 1989 *Sov. Phys. JETP* **68** 101–3
[24] Rößler U, Bogdanov A and Pfleiderer C 2006 *Nature* **442** 797–801
[25] Rybakov F N, Borisov A B, Blügel S and Kiselev N S 2015 *Phys. Rev. Lett.* **115** 117201
[26] Zheng F *et al* 2018 *Nat. Nanotechnol.* **13** 451–5
[27] Taguchi Y, Oohara Y, Yoshizawa H, Nagaosa N and Tokura Y 2001 *Science* **291** 2573–6
[28] Shindou R and Nagaosa N 2001 *Phys. Rev. Lett.* **87** 116801
[29] Schulz T, Ritz R, Bauer A, Halder M, Wagner M, Franz C, Pfleiderer C, Everschor K, Garst M and Rosch A 2012 *Nat. Phys.* **8** 301–4
[30] dos Santos Dias M, Bouaziz J, Bouhassoune M, Blügel S and Lounis S 2016 *Nat. Commun.* **7** 13613
[31] Hanke J P, Freimuth F, Blügel S and Mokrousov Y 2017 *Sci. Rep.* **7** 41078
[32] Bode M, Heide M, Von Bergmann K, Ferriani P, Heinze S, Bihlmayer G, Kubetzka A, Pietzsch O, Blügel S and Wiesendanger R 2007 *Nature* **447** 190–3
[33] Ferriani P, von Bergmann K, Vedmedenko E, Heinze S, Bode M, Heide M, Bihlmayer G, Blügel S and Wiesendanger R 2008 *Phys. Rev. Lett.* **101** 027201
[34] Hermenau J, Brinker S, Marciani M, Steinbrecher M, dos Santos Dias M, Wiesendanger R, Lounis S and Wiebe J 2019 *Nat. Commun.* **10** 2565
[35] Yoshida Y, Schröder S, Ferriani P, Serrate D, Kubetzka A, von Bergmann K, Heinze S and Wiesendanger R 2012 *Phys. Rev. Lett.* **108** 087205
[36] Takagi R, White J S, Hayami S, Arita R, Honecker D, Rønnow H M, Tokura Y and Seki S 2018 *Sci. Adv.* **4** eaau3402
[37] Romming N, Pralow H, Kubetzka A, Hoffmann M, von Malottki S, Meyer S, Dupé B, Wiesendanger R, von Bergmann K and Heinze S 2018 *Phys. Rev. Lett.* **120** 207201
[38] Heinze S, von Bergmann K, Menzel M, Brede J, Kubetzka A, Wiesendanger R, Bihlmayer G and Blügel S 2011 *Nat. Phys.* **7** 713
[39] Fert A and Levy P M 1980 *Phys. Rev. Lett.* **44** 1538–41
[40] Levy P M and Fert A 1981 *Phys. Rev.* B **23** 4667–90
[41] Crépieux A and Lacroix C 1998 *J. Magn. Magn. Mater.* **182** 341–9
[42] Papanikolaou N, Zeller R and Dederichs P H 2002 *J. Phys.: Condens. Matter.* **14** 2799–823
[43] Vosko S H, Wilk L and Nusair M 1980 *Can. J. Phys.* **58** 1200–11
[44] Bauer D S G 2014 Development of a relativistic full-potential first-principles multiple scattering Green function method applied to complex magnetic textures of nano structures at surfaces *PhD Thesis* RWTH Aachen
[45] Błoński P and Hafner J 2009 *J. Phys.: Condens. Matter.* **21** 426001
[46] Giannozzi P *et al* 2017 *J. Phys.: Condens. Matter.* **29** 465901
[47] Corso A D 2014 *Comput. Mater. Sci.* **95** 337–50
[48] Perdew J P, Ruzsinszky A, Csonka G I, Vydrov O A, Scuseria G E, Constantin L A, Zhou X and Burke K 2008 *Phys. Rev. Lett.* **100** 136406
[49] Jülich Supercomputing Centre 2018 *J. Large-scale Res. Facil.* **4** A132
[50] Ujfalussy B, Wang X D, Nicholson D, Shelton W, Stocks G, Wang Y and Gyorffy B 1999 *J. Appl. Phys.* **85** 4824–6
[51] Lebedev V I and Laikov D 1999 *Dokl. Math.* **59** 477–81
[52] Drautz R and Fähnle M 2004 *Phys. Rev.* B **69** 104404
[53] Drautz R and Fähnle M 2005 *Phys. Rev.* B **72** 212405
[54] Tewari S, Belitz D and Kirkpatrick T R 2006 *Phys. Rev. Lett.* **96** 047207
[55] Lászlóffy A, Rózsa L, Palotás K, Udvardi L and Szunyogh L 2019 *Phys. Rev.* B **99** 184430
[56] Grytsiuk S, Hanke J P, Hoffmann M, Bouaziz J, Gomonay O, Bihlmayer G, Lounis S, Mokrousov Y and Blügel S 2019 arXiv:1904.02369